Frequency-Domain Design/Analysis of Robust Flight Control Systems

Ronald A. Hess
Dept. of Mechanical and Aeronautical Engineering
University of California
Davis, CA 95616-5294
USA

rahess@ucdavis.edu

ABSTRACT

The design of aircraft flight control systems that are robust to the effects of uncertainties or sudden changes in the dynamics of the vehicle under control is a topic of continuing interest to both the civilian and military communities. Potential design applications range from large-scale piloted aircraft to small, autonomous, nano-scale uninhabited air vehicles. The use of frequency-domain control system synthesis techniques in these applications can render transparent the design tradeoffs that need to be considered throughout. A frequency-domain approach to the design of sliding mode control (SMC) systems is discussed. True sliding behaviour with infinite-frequency control switching is, of necessity, replaced by control inputs that are continuous in nature, leading to a more accurate description of the technique as pseudo-sliding mode control. The ability of asymptotic observers to address the problem of parasitic dynamics in SMC designs is emphasized. In aerospace applications, these parasitic dynamics are typically associated with the actuators driving the control effectors. A brief introduction of SMC theory is presented, followed by a description of a step-by-step design procedure for the synthesis of multi-input, multi-output SMC designs in the frequency domain. A series of flight-control design examples follows, covering vehicles that range in size from a large, piloted bomber aircraft to a so-called nano-scale autonomous unmanned air vehicle.

1.0 INTRODUCTION

The specific functions that a flight control system will typically be required to perform are succinctly described in a classic textbook in the area [1]. These functions are:

- Provide vehicle stability and controllability
- Reduce the “effective” order of the vehicle dynamics
- Adjust the “effective” vehicle dynamic response
- Provide specified command-response relationships
- Reduce the effects of unwanted inputs and disturbances
- Suppress the effects of vehicle and component variations and uncertainties
- Improve linearity
- Modify or eliminate vehicle cross-coupling effects

Hess, R.A. (2007) Frequency-Domain Design/Analysis of Robust Flight Control Systems. In *System Control Technologies, Design Considerations & Integrated Optimization Factors for Distributed Nano UAV Applications* (pp. 3-1 – 3-56). Educational Notes RTO-EN-SCI-175, Paper 3. Neuilly-sur-Seine, France: RTO. Available from: http://www.rto.nato.int.

The ability of a control system synthesis technique to address these functions is of obvious importance. The ability to do so with transparency, i.e. to provide the control system engineer with insight as to how design decisions affect each functional requirement is equally vital. Indeed, the importance the role which the latter attribute plays in the design process has led to a recent emphasis on "bridging the gap" between theory and practice [2]. Quantitative Feedback Theory [3] is one synthesis procedure that addresses the functions just outlined and does so with an eye toward transparency. The approach to be discussed herein, may provide another. It is worth emphasizing that the requirements just outlined are common to the design of flight control systems for *any* vehicle, regardless of size, mission, or the level of autonomy required.

The requirement summarized by the sixth bullet above has been of particular interest to researchers of late. Indeed, the importance of suppressing effects of variations in vehicle dynamics (such as might occur with battle damage) has seen the birth of "reconfigurable" flight control system design has a legitimate sub-discipline in the field [4]. The novel and challenging requirement here is that of dealing with system changes that are large and sudden i.e., those that may not be manageable with static, non-adaptive designs. Since many modern aircraft also exhibit dynamic modes that are unstable without control augmentation, the necessity of rapid adaptation to these large system variations adds another challenge to functional requirements. In addition, in considering "nano-scale" vehicles, robustness to damage must be obtainable with relatively modest computational power, thus eliminating designs requiring failure detection, failure isolation and control reconfiguration.

The research described in [5] was an attempt to meet the challenges of suppressing the effects of large and sudden changes in vehicle dynamic characteristics with a design technique that obviated failure identification, isolation and control system adaptation. The technique was essentially a frequency-domain approach to the creation of pseudo-sliding mode control (SMC) systems that capitalized on the (near) invariance of these designs to matched uncertainty in the dynamics of the vehicle being controlled [6]. Like all control synthesis techniques, the proposed pseudo-SMC approach came with a cost, in this case, high-frequency control activity. This is not a surprising result, given the lineage of the design. It is derived from true sliding mode control which entails infinite frequency switching of the control inputs to maintain the system state on the sliding manifold [6].

The frequency-domain nature of the pseudo-SMC design approach arises in the manner in which the sliding manifolds are chosen: Well known loop-shaping techniques are employed that yield loop transmissions with desirable characteristics. These are best summarized by the "primary rule-of-thumb" for frequency-domain synthesis [7]: *Find or create a fair stretch of –20 dB/dec slope for the Bode plot amplitude ratio of the loop transmission, and then make it the crossover region by putting the 0 dB line through it.* While not always stated as succinctly as in the previous sentence, this prescription is found in many of the texts on control system design, e.g., [8]. The second element in the frequency-domain application is the manner in which the eigenvalues of asymptotic estimators are chosen. As mentioned in the preceding, these estimators are utilized to reduce the sensitivity of SMC design approaches to the effects of parasitic dynamics [6].

The presentation is outlined as follows: Section 2 will briefly describe the general SMC design philosophy. Section 3 will describe the frequency-domain approach outlined in the preceding paragraph. Section 4 will provide a necessary description of models of the human pilot that will be utilized in some of the computer simulations of the SMC design examples that are presented in Section 5. Section 6 is a discussion of the results and Section 7 provides a summary and acknowledgments.

2.0 SLIDING MODE CONTROL SYSTEM DESIGN

2.1 Introduction

Much of what follows was first presented in [5]. In its purest incarnation, SMC offers a control system with instantaneous and complete "adaptation" to what is termed *matched uncertainty*, i.e., SMC requires no failure detection/isolation, control re-allocation, parameter identification and system reconfiguration. The fundamental concepts describing SMC were first seen in the Russian literature in the 1930s. It was not until the 1970s that the ideas of SMC appeared in the Western literature when a text by Itkis [9], and a survey paper by Utkin [10] appeared. By the early 1990s, applications of SMC became numerous. These included robot control, motor control, and aircraft and spacecraft control. A recent text is devoted entirely to SMC design [11].

Consider the uncertain system with *m* inputs and *n* states described by:

$$\dot{\mathbf{x}}(t) = \mathbf{A}(\mathbf{x}, t) + \mathbf{B}(\mathbf{x}, t)\mathbf{u}(t) + \mathbf{E}\xi(\mathbf{x}, t) \tag{1}$$

where $\mathbf{A} \in \Re^{n\times n}$ and $\mathbf{B} \in \Re^{n\times m}$; **B** is full rank, $1 \le m < n$, and R(**E**) $\subset$ R(**B**). The matrix $\mathbf{E} \in \Re^{n\times l}$ is known and the function $\xi : \Re_+ \times \Re^n \mapsto \Re^l$ is unknown and represents the parameter uncertainty or nonlinearities present in the system. **E**ξ(**x**,t) is assumed to be bounded by some known functions of the state. Any uncertainty in this form with R(**E**) $\subset$ R(**B**) is called matched uncertainty. The objective is to define: *m* switching functions, represented in vector form as $\boldsymbol{\sigma}(x)$, and a variable structure control

$$\mathbf{u}(\mathbf{x}, t) = \boldsymbol{\rho}\,\mathrm{sgn}(\boldsymbol{\sigma}) \tag{2}$$

such that any state outside the switching surface is driven to the surface in finite time and remains on this surface for all subsequent time (the so-called sliding mode). The line (or hypersurface or manifold) that describes $\boldsymbol{\sigma} = \mathbf{0}$ defines the transient response of the system during the sliding mode (the so-called sliding surface). There are three basic properties about SMC that can be observed [11]:

(a) During the sliding mode, the trajectory dynamics are of a lower order than the original model.

(b) While on the sliding mode, the system dynamics are solely governed by the parameters that describe the line $\boldsymbol{\sigma} = \mathbf{0}$ and are insensitive to the uncertainty function ξ(**x**,t) in Eq. 1

(c) The trajectory of the sliding mode is one that is not inherent in either of the two control structures alone.

It is item (b) immediately above that summarizes the invariance possible with SMC. Nothing has been said thus far about guaranteeing that the system will reach the sliding surface and remain on the surface once it is on it. Existence of the sliding mode requires stability of the state trajectory to the surface, or at least in some neighborhood surrounding the surface, known as the *region of attraction*. In order for the sliding surface to be attractive, the trajectories of $\sigma(t)$ must be directed towards it. This can be stated succinctly as requiring

$$\dot{\boldsymbol{\sigma}}^{\mathrm{T}}(t)\boldsymbol{\sigma}(t) < 0 \tag{3}$$

which is called the *reachability condition*.

2.2 Sliding Mode Design - Multi-Input, Multi-Output Systems

There are many SMC design approaches in the literature. Indeed, an almost limitless variety of control strategies can achieve sliding behaviour. The approach to be followed herein is based upon feedback linearization, as discussed in [12]. The two major assumptions are involved in this approach are:

(a) the system is square, i.e., an equal number of inputs and outputs, and

(b) the system is feedback linearizable, i.e., no transmission zeros lie in the right half plane and uncontrollable states must be stable.

If the system in question meets these criteria, it is possible to decouple the outputs with the given inputs. This transforms a multi-input, multi-output (MIMO) design into *m* single-input, single-output (SISO) designs, where *m* is the number of inputs or outputs.

Consider a non-linear, square MIMO system

$$\begin{aligned} \dot{\mathbf{x}} &= \mathbf{A(x)} + \mathbf{B(x)}\,\mathbf{u} \\ \mathbf{y} &= \mathbf{C(x)} \end{aligned} \tag{4}$$

where $\mathbf{x} \in \Re^n$, $\mathbf{y} \in \Re^m$, $\mathbf{u} \in \Re^m$. Assume the functions $\mathbf{A(x)}$, $\mathbf{C(x)}$ and columns $b_i(\mathbf{x})$ $\forall i = \overline{i, m}$ of the matrix $\mathbf{B(x)} \in \Re^{n\times m}$ are smooth vector fields. Further, assume the system is completely linearizable in a reasonable domain $\mathbf{x} \in \mathbf{\Gamma}$. The control system will be designed to track a real-time reference profile, $\mathbf{y}_r(t)$. First, *m* independent sliding surfaces or manifolds are created.

$$\sigma_i = e_i^{(r_i-1)} + c_{i,r_i-2}e_i^{(r_i-2)} + \ldots + c_{i,1}e_i^{(1)} + c_{i,0}e_i \quad \forall i = 1,m \tag{5}$$

Note that these have orders exactly one less than the relative order r_i for the corresponding state variable, where relative order refers to the order of the derivative of y_i necessary to ensure that a term containing an element of **u** appears.

Here $e_i = y_{r,i}(t) - y_i(t)$, $e_i^{(j)} = \dfrac{d^j e_i}{dt^j}$. The coefficients $c_{i,j}$, $\forall i = 1,m$ and $\forall j = 0, r_i - 2$, are design parameters which can be chosen in a number of ways, e.g., to achieve the desired eigenvalue placement of the decoupled differential equations of the output variables. In a later section, a frequency-domain approach to the selection of the c_i will be presented. It is also common to include an integral term, $c_{i,-1}\int e_i d\tau$, in the sliding equations to account for potential steady state error which can occur when utilizing a sliding mode boundary layer. The control law that can be used is

$$u_i = \rho_i \,\mathrm{sgn}(\sigma_i) \tag{6}$$

In order to prove system stability one can refer to the scalar version of Eq. 3. The parameter ρ_i will appear in

the expression for $\dot{\sigma}_i$. One then determines the minimum ρ_i that will provide global attractiveness to the sliding surface in finite time, i.e., that ensures that $\dot{\sigma}_i \sigma_i < 0$. However, in systems in which a human agent is active in outer-loop control, such in piloted aircraft, this approach is problematic, as expressions for σ and $\dot{\sigma}$ will be an unknown function of the pilot's control inputs

2.3 Implementation Issues

While very attractive from a robustness standpoint, serious implementation issues must be addressed in SMC applications. The most serious of these issues is the infinite frequency switching that occurs when the control law of Eq. 6 is used in a control system. The switching has been called "chatter" by some researchers, although strictly speaking, chatter refers to a related (and undesirable) phenomenon in which the state trajectories chatter along the sliding manifold. The simplest and most common approach for the elimination of infinite frequency switching in the control law is use of a so-called boundary layer in which the signum function of Eq. 6 is replaced by an approximation, e.g., a saturation element. The result of using such an element is that the control becomes continuous and the states become attracted to a small layer surrounding the switching surface. Since the ideal sliding motion is lost, the resulting system is often referred to as pseudo-sliding. In addition, when a boundary layer is introduced, invariance is lost, although the system still retains much of its robustness. Ensuring that sufficient robustness remains in the design constitutes the major challenge of the research to be described.

2.4 Unmodelled parasitic dynamics

Unmodelled parasitic dynamics refer to dynamics of the vehicle that are typically neglected in the design procedure. In flight control applications, these can include actuator dynamics. Unfortunately, SMC designs are very sensitive to the effects of unmodelled parasitic dynamics [6]. The simplest solution to the actuator problem would appear to be the inclusion of actuator models as part of the vehicle model. However, including actuator dynamics will increase the relative order of the system, and, as Eq. 5 indicates, the order of the manifolds. This means, for example, that inclusion of a second order actuator model will require that at least two derivatives of the system output in the definition of the sliding surfaces. In practice, measurement noise makes this approach very unattractive. A number of approaches have been offered in the literature for dealing with the effects of parasitic dynamics.

(a) dynamic boundary layers in which the boundary layer thickness is continuously adjusted to keep the controller operating in the linear region,

(b) disturbance compensation in which an SMC disturbance estimator is employed,

(c) SMC design with a prefilter in which actuator dynamics are incorporated as a prefilter to the SMC

(d) observer-based SMC in which an asymptotic observer is placed in the feedback path for the SMC.

The observer-based approach will be adopted in the research to be described. This decision is based upon the relative simplicity of this technique and the fact that it is easily amenable to a frequency domain description. As will be demonstrated, separate observers for each feedback variable (each decoupled control loop in a MIMO system) can be employed in the design.

The observer equation is given by

$$\dot{\hat{\mathbf{x}}} = \mathbf{A}\hat{\mathbf{x}} + \mathbf{B}\mathbf{u} + \mathbf{K}_e(\mathbf{y} - \mathbf{C}\hat{\mathbf{x}}) \tag{7}$$

where $\mathbf{K}_e$ is the observer gain matrix. The **A**, **B**, and **C** matrices are linearized versions of the matrices appearing in Eq. 4. Observer eigenvalues are typically selected as real and (nearly) identical. The latter requirement is invoked to prevent algorithmic difficulties that may arise in attempting to place identical eigenvalues. The eigenvalues can be shown to affect SMC performance in the following manner: Large observer eigenvalues increase the robustness of the SMC design to variations in vehicle characteristics but also increase the susceptibility of the design to the deleterious effects of unmodelled parasitic dynamics. Small observer eigenvalues decrease the robustness of the SMC design to variations in vehicle characteristics, but also decreases the susceptibility of the design to the effects of unmodelled parasitic dynamics. The SMC approach to be described can also utilize "reference model hedging" [5],[13] to permit large observer eigenvalues while minimizing susceptibility to parasitic dynamics.

2.4 Reference Model Hedging

Figure 1 shows a SISO control system including the asymptotic observers and reference model hedging as just outlined. The "plant" in Fig. 1 is described by the **A** and **B** matrices of Eq. 4. The variable "z" represents a measurable system output that may or may not be the desired response variable "y". Note that here and elsewhere, the output of the SMC system will be denoted $\mathbf{u}_c$ while the output of actuators is denoted $\mathbf{u}_a$. The variables denoted $\hat{y}_i$ represent estimates of the elements of the output vector **y** in Eq. 7. In Fig. 1, G_h represents a model of the vehicle.

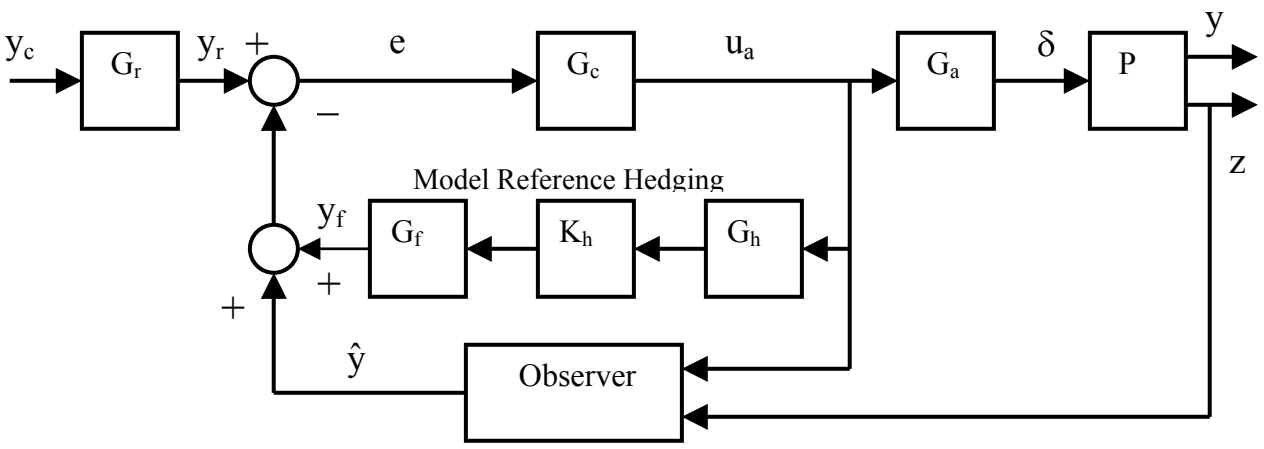

Figure 1: A SISO SMC system with observer and reference model hedging

In the frequency domain approach to be described, G_h is generalized and simplified to the following form:

$$G_h = \frac{a_0}{(s^{r_i+1} + a_{r_i} s^{r_i} + \cdots + a_0)} \tag{8}$$

where r_i is the relative order of the output variable of interest. Likewise, the filter G_f is a high-pass filter of the form

$$G_f = \frac{s}{s+b} \tag{9}$$

The selection of the parameters in Eqs. 8 and 9 is based upon a Bode diagram of the hedge transfer function $\hat{y}_h / y_c$ [13]. Referring to Fig. 1, $G_h G_f$ is created so that the magnitude portion of its Bode diagram exhibits the following characteristics: +20 dB/dec slope at low frequencies, $-20r_1$ dB/dec slope at frequencies where the (neglected) actuator dynamics distort the magnitude curve of $\hat{y}_h / y_r$, (r_1 = the relative order of system without parasitic dynamics) and, $-20(r_1+1)$ dB/dec slope at high frequencies.

The gain K_h is then varied until the transfer function $\hat{y}_h / y_r$ in Fig. 1 closely approximates that for the vehicle without parasitic dynamics while employing as large as eigenvalues as possible in the corresponding observer. The similarity between this generalized hedging and loop transfer recovery [14] as utilized in linear quadratic gaussian control designs should be noted.

3.0 SMC FREQUENCY-DOMAIN DESIGN PROCEDURE

An SMC step-by-step design procedure can now be presented in fashion. As part of the procedure, one creates a computer simulation of the system. Here, this is accomplished using MATLAB® and Simulink®. The steps are directed toward the single loop of a SISO system or any single loop of a MIMO system. In either case, only a scalar sliding surface definition is involved. As will be seen, a frequency-domain interpretation of the sliding surfaces is used. The following borrows heavily on the discussion in [15].

(1) Plant Definition: A vehicle model is chosen. It may or may not include reduced-order actuator model(s) per the designer's choice. A 'limit frequency' is defined above which parasitic dynamics become a concern.

(2) Reference Model: A reference model is chosen. If directed toward the design of piloted vehicles, a reference model selection should be predicated upon achieving Level 1 handling qualities [16].

(3) Sliding Surface Definition: The desired feedback structure is determined, e.g., a pitch rate command flight control system. If there are multiple actuators serviced by each pseudo-control produced by the SMC system, a control distribution matrix must be created, e.g., using the pseudo-inverse approach of [13]. The sliding manifold can then be created using the following rules:

(a) σ is derived from a tracking error expression Eq. 5. An integral term is also included that compensates for the addition of the boundary layer.

$$\sigma = e(t)^{r_i-1} + c_{r_i-2} e(t)^{r_i-2} + \ldots + c_0 e(t) + c_{-1} \int e(t)dt \tag{10}$$

(b) Equation 10 can be transformed to the Laplace domain and expressed as

$$u_c(s) = \frac{\rho}{\varepsilon}\sigma = K_\rho\left(s^{r_1-1} + c_{r_1-2}s^{r_1-2} + \ldots + c_0 + \frac{c_{-1}}{s}\right)e(s) \tag{11}$$

In the frequency domain, the c_i are chosen to produce desirable properties around the crossover frequency of the loop transmission defined by Eq. 11, i.e., a K/s-like transfer function [7],[8]. This will always be possible to achieve since enough derivatives are included in Eq. 10 (and powers of s in Eq. 11) to produce the desired shape at frequencies at least as high as the limit frequency. K_ρ is also obtained in this step and determines the crossover frequency. Since the signum function will be replaced by a saturation element with a ±1 limit, K_ρ represents the largest possible control output of the SMC. Thus, to use the entire range of the actuator suite in question, the minimum K_ρ must be equal to or greater than the position limit of the actuator with the largest position limit. Also note that the crossover frequency obtained in this will typically be very large and well beyond the limit frequency. This is of no concern at this juncture.

(4) Sliding Behaviour: The existence of the sliding mode is now be confirmed. Here the signum function is used without a boundary layer in a computer simulation of the system. A test input is applied to the SMC system, typically consisting of a random, or random-appearing signal with an RMS value representing the upper limit of what will be expected in practice. Infinite switching in the SMC output $u_c(t)$ should be observed in addition to $\sigma(t) \cong 0$. Note that no observer(s), no actuator models more complex than those selected in step (1), no reference models, and no hedging are included at this stage. In addition, no outer feedback loops are closed. If sliding behaviour (infinite switching and $\sigma(t) \cong 0$) is not observed, K_ρ is increased until it is.

(5) Boundary Layer: A boundary layer is introduced using a saturation element with limits of unity. Measurement noise should be included. The boundary layer thickness ε is increased until no infinite switching is observed using the test input while maintaining near perfect tracking as seen in $\sigma(t) \approx 0$. This should be possible even with large variations in plant dynamics. Modifying ρ may be necessary in this step. If ε increases above 1, ρ is increased proportionally to maintain a constant $\rho/\varepsilon = K_\rho$.

(6) Parasitic Dynamics: The dynamics of the operational actuators are now included in the computer simulation of the system. This will almost surely cause the system to be unstable.

(7) Observers: The design of the observers is of critical importance to the tracking performance and robustness of the entire system. The poles of this observer typically lie between the limit frequency and the bandwidth of the reference model. In the MIMO case, an independent observer on each feedback channel can significantly improve tracking performance and robustness by allowing different observer eigenvalues in each loop. The eigenvalues are typically chosen to be real, and nearly equal. One method for choosing the eigenvalues is to create an "equivalent" unity-feedback loop transmission defined as

$$L_{eq}(s) = \frac{\frac{C}{R}(s)}{1 - \frac{C}{R}(s)} \tag{12}$$

This is shown in Fig. 2. The eigenvalues are then chosen so as to produce acceptable gain and phase margins

in the $L_{eq}(s)$ just defined.

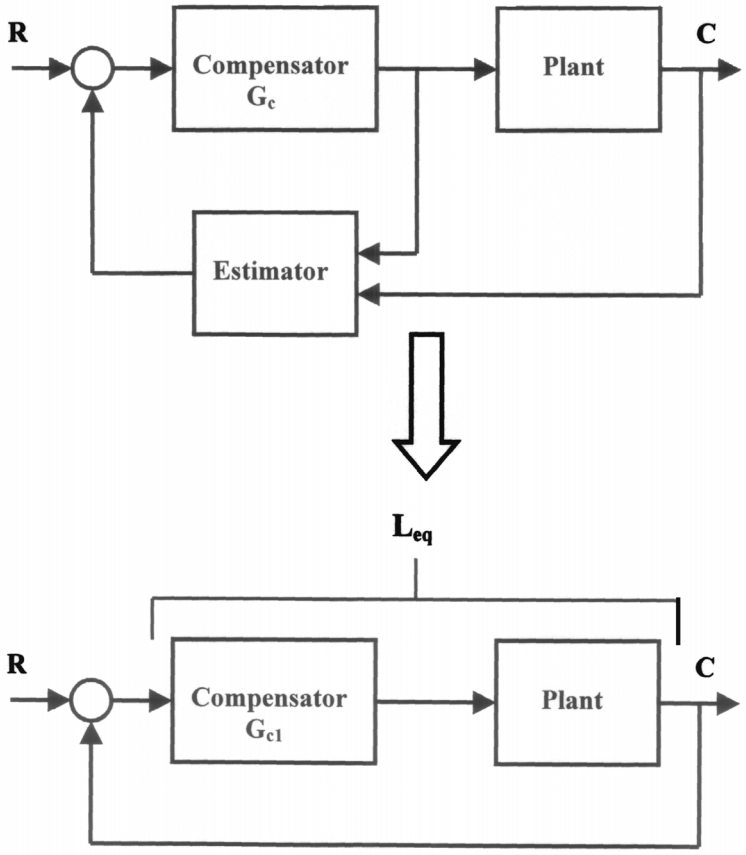

Figure 2 Defining the equivalent, unity-feedback loop transmission

(8) Hedging: The model reference hedging is designed in the frequency domain as described in Section 2.4

(9) The observer of step (7) can be scheduled with vehicle flight condition. Typically, this will not require changes in the definitions of the controller designed in steps (3-5). The vehicle dynamics in the region of the open-loop crossover frequencies will be nearly invariant with flight condition. This is attributable to the large crossover frequencies employed in the SMC loops and that fact that crossover occurs in the frequency region that defines the relative order of each loop.

(10) Reduced-order Model Actuators: If desired, and if not included in step (1), actuator models may be included in the design, but of lower order than the actual, operational actuators. Steps (3)-(9) are repeated. As a rule of thumb, the bandwidth of the lower-order actuators should be chosen to be approximately 60% of the operational ones. This step can improve system robustness by including a lower-order model of parasitic dynamics without requiring excessive differentiation of the error signal in the sliding surface definition of Eq. 10.

4.0 CONTROL-THEORETIC HUMAN PILOT MODELS

4.1 Pilot Model Formulation – Single Axis

The evaluation of flight control laws for piloted aircraft inevitably include performance and handling qualities evaluations. When applied to systems that will, over some portion of their operational envelope, be subject to manual control, the results of the synthesis procedure outlined in Section 2 should also be subject to such evaluation. In an analytical framework, this means relying upon mathematical models of the human pilot. The pilot model to be discussed here is the control-theoretic representation known as the Structural Model of the human pilot [17]. The model is shown in Figure 3, in a single-axis application.

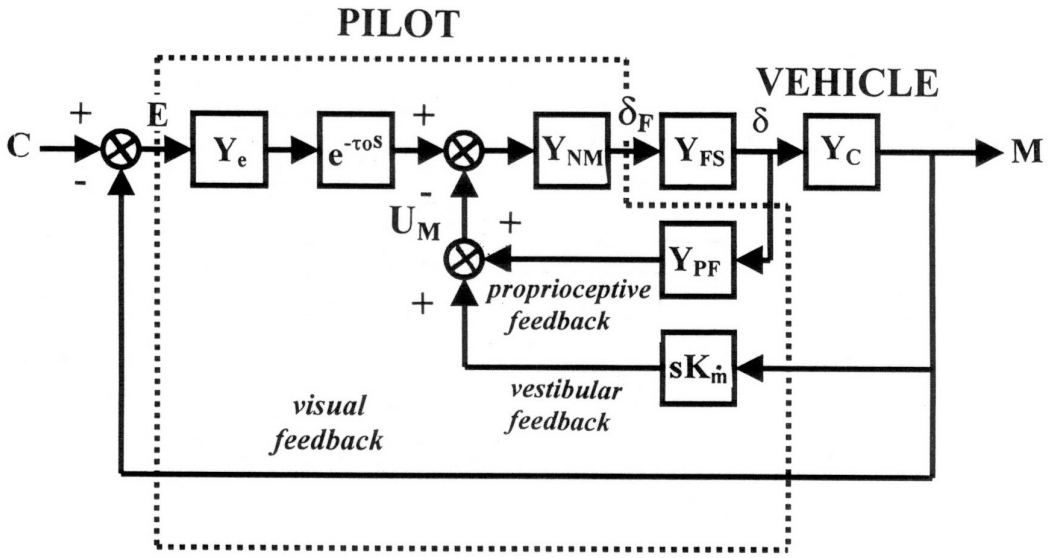

Figure 3: A Structural Model of the human pilot

A set of rules have postulated for selecting the model parameters shown in Fig. 3. They are described in [17] and briefly summarized in what follows.

For most applications, the vestibular feedback loop can be ignored. This is not to imply that these cues are unimportant, but rather that the fundamental equalization characteristics of the human can be captured using only the visual and proprioceptive loops [18]. For the great majority of applications, the proprioceptive feedback element Y_{PF} takes one of the following forms:

$$Y_{PF} = K(s+a), \quad K \quad \text{or} \quad K/(s+a) \tag{13}$$

with the particular form in Eq. 13 dependent upon the form of the vehicle dynamics (including flight control system) in the region of the open-loop crossover for the control axis in question. For selecting the form of Eq. 13, this crossover frequency is selected as 2.0 rad/sec. That is, with $Y_c(s)$ representing the transfer function of

the "effective" vehicle (aircraft + flight control system)

$$\frac{Y_c(j\omega)}{Y_{PF}(j\omega)} \approx \frac{K_1}{(j\omega)} \text{ for } \omega \approx \omega_c = 2 \text{ rad/sec and } K_1 \text{ arbitrary} \tag{14}$$

The element Y_{NM} is a simplified model of the neuromuscular system in the pilot's limb that is effecting control and is represented by

$$Y_{NM}(s) = \frac{10^2}{(s^2 + 14.14s + 10^2)} \tag{15}$$

It is obvious that Eq. 15 is a simplification. Indeed, more detailed models of the pilot's neuromotor dynamics have been identified in the literature, e.g., [19], [20]. The element Y_{FS} represents the (linear) dynamics of the force/feel system of the cockpit inceptor in question. Due to the manner in which the gain K in Eq. 13 is chosen, the particular units on Y_{FS} are not important, assuming of course that the force/displacement characteristics are within the capability of the human. The gain K in Eq. 13 is chosen by determining the value that will yield a minimum damping ratio of 0.15 in the poles of the inner-most control loop in Fig. 3. The time delay τ_0 is set to 0.2 sec. Finally, the element Y_e is selected as

$$Y_e = \frac{K_e[s + (\omega_c / 2)]}{s} \tag{16}$$

The low-frequency integration apparent in Eq. 16 omitted in many applications. The integration is sometimes employed in modelling piloting tasks in which deterministic pilot input commands are used, e.g. [21].

4.2 Analytical Handling Qualities Assessment

Estimation of the handling qualities of a pilot/vehicle system can also be undertaken with the model of Fig. 3, as discussed in [17]. Since such assessment is not the central theme of this Lecture Series, this capability will only be touched upon herein. With the pilot model selected as described in the preceding section, a Handling Qualities Sensitivity Function (HQSF) can be defined as

$$\text{HQSF} = \frac{1}{|K_e|}\left|\frac{U_M}{C}(j\omega)\right| \tag{17}$$

where U_M and C are shown in Fig. 3. This function is plotted on a linear scale vs ω and handling qualities levels for the piloting task at hand are predicted based upon which of two pre-determined handling qualities bounds are violated in the figure. The genesis of this procedure is given in [17]. Figure 4 shows a typical HQSF where Level 1 handling qualities have been predicted.

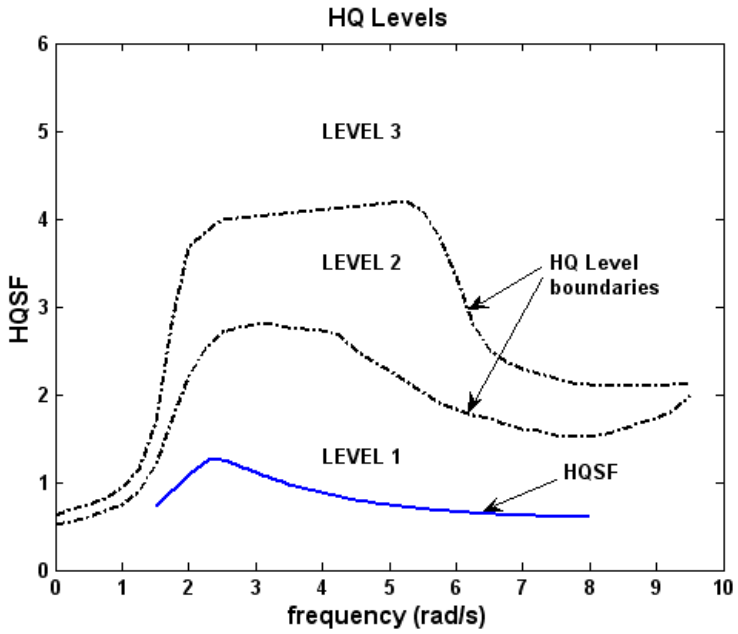

Figure 4: The Handling Qualities Sensitivity function with Level 1 handling qualities predicted

4.1 Pilot Model Formulation – Multi-Axis, Multi-Loop

Figure 5 shows a multi-loop application of the pilot modelling procedure, here for a hovering rotorcraft.

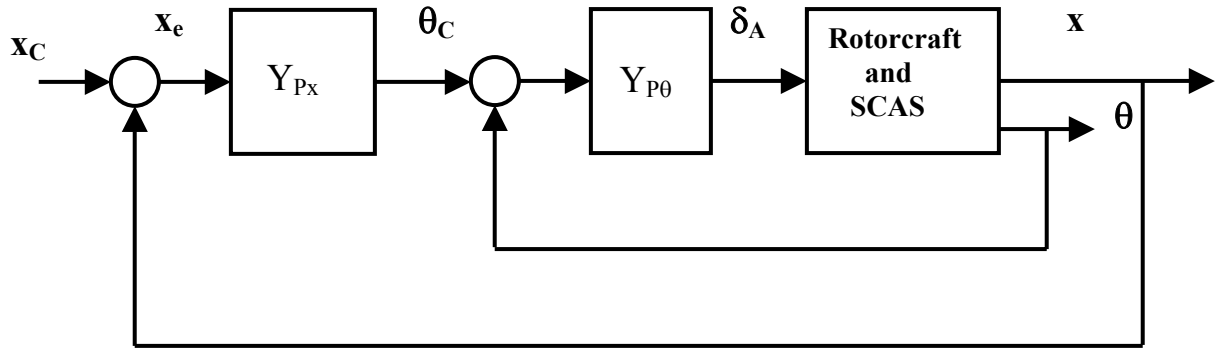

Figure 5: A multi-loop pilot/vehicle system.

Here, δ_A represents the longitudinal cyclic input, θ represents the vehicle pitch attitude, and x the vehicle longitudinal displacement. Yp_θ represents the Structural Pilot Model of Fig. 3 and Yp_x represents the pilot equalization activity in the outer, position loop. Outer loop pilot models such as Yp_x are typically very simple in form, e.g., consisting of, at most, a gain and lead term. Yp_x is chosen so that the transfer function

$$\frac{X}{X_e}(s) \approx \frac{\omega_{c\theta}/3}{s} \tag{18}$$

where ωc_θ is the crossover frequency of the inner, pitch-attitude control loop (nominally 2 rad/sec). Similar pilot vehicle control loops can be created for the roll/lateral position loops and the heave-rate/vertical position loops, e.g. [22]. Handling qualities sensitivity functions are obtained for each control axis, with the remaining control loops closed with the pilot models. The HQSF indicating the poorest handling qualities (highest handling qualities level) is used to predict the overall, "task-independent" handling qualities. In addition, and as demonstrated in [22] "task-dependent" handling qualities levels can be predicted based upon the performance of the modelled pilot/vehicle system in specific piloting tasks in which performance requirements have been specified.

5.0 EXAMPLES OF THE SMC DESIGN PROCEDURE

Mathematical models of five "aircraft" will be utilized in the examples to follow. They are (1) a large intercontinental bomber, (2) a innovative control effector fighter aircraft (ICE), (3) a 21 inch diameter ducted-fan UAV, (4) a 9-inch ducted-fan UAV, and (5) a 2.26 inch mesicopter UAV. Figure 6 is a logarithmic plot comparing the size (span) and weight of these five vehicles.

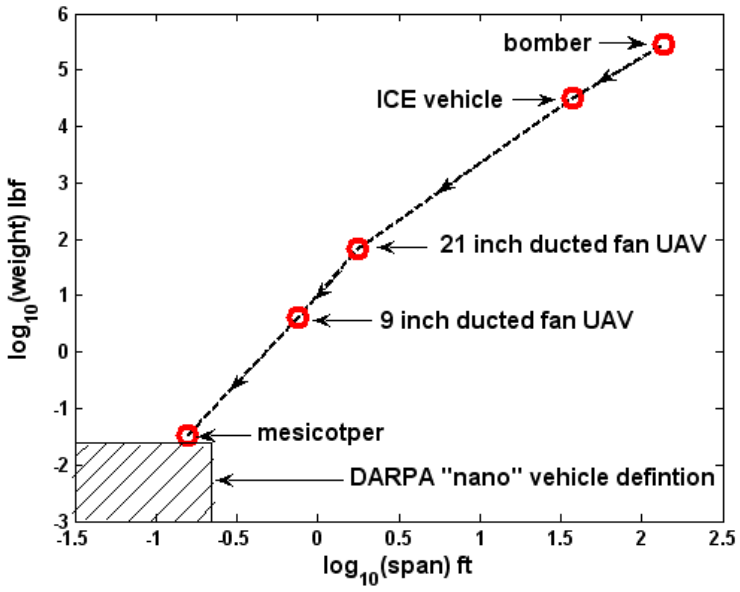

Figure 6 Size and weight comparison of the example vehicles

5.1 A Longitudinal Pitch-Attitude Control System for a Large, Flexible Aircraft

5.1.1 The SMC Design

The aircraft that is the subject of this example is shown in Fig. 7. The vehicle represents a long-range bomber whose aeroelastic characteristics have been analytically modified. Details of the vehicle model can be found

in [23]. The only control effector being considered is the horizontal stabilator. As modelled, the vehicle exhibits three structural modes, whose natural frequencies are shown in Table 1. The mode shapes are indicated in Fig. 8.

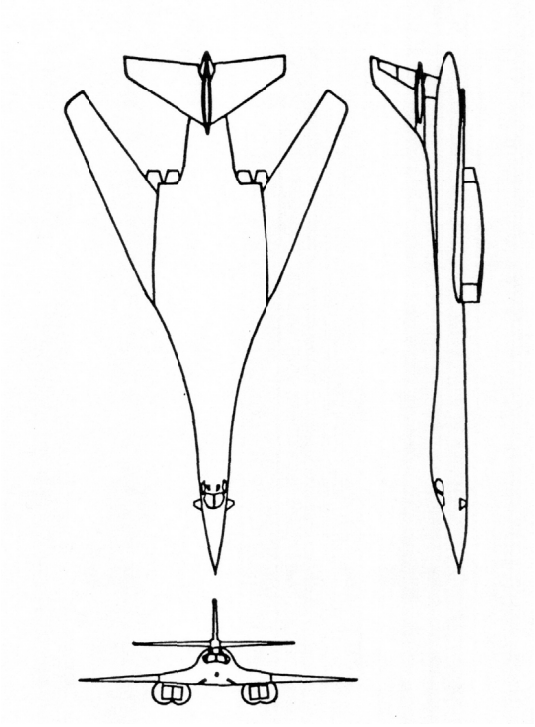

Figure 7 Geometry of the flexible aircraft model

Table 1: Structural Mode Vibration Frequencies of Study Vehicle

Mode 1	Mode 2	Mode 3	Mode 4
12.57	14.07	21.17	22.05
(rad/sec)	(rad/sec	(rad/sec)	(rad/sec)

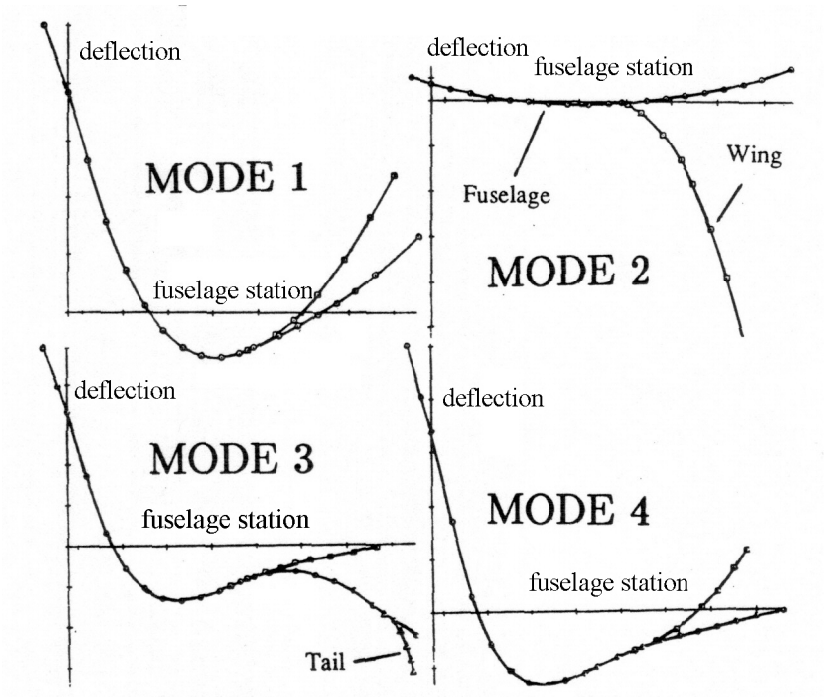

Figure 8 Structural Mode Shapes from [21]

The mode shapes of the modes are shown in Fig. 8 as they appeared in [23]. Scales for the abscissae and ordinates of Fig. 8 for the first two structural modes are provided in [24]. Ordinate scales for modes 3 and 4 were not available to the authors and had to be assigned for this study. That is, the scaling of the ordinates for modes 3 and 4 were assumed to be identical to that for modes 1 and 2. From a modelling standpoint, these represent conservative estimates. It should be noted that, with this assumption, the Bode plot of the vehicle pitch rate at the cockpit to stabilator deflection provided an acceptable match to that reported in [23]. An amplitude and rate-limited actuator model will be included in the design. Second-order actuator dynamics were assumed with a break frequency of 35 rad/sec were assumed. Figure 9 shows the Bode plot of the transfer function $q_{cp}(s)/\delta_{st}(s)$, i.e., the pitch-rate at the cockpit due to stabilator deflection (excluding actuator dynamics). The primary reason for choosing this example was to demonstrate that the high-bandwidth nature of the SMC approach, with the concomitant large control activity, does not necessarily limit applications to vehicles with minimal structural flexibility.

Two important design considerations must be mentioned at this point: First, for the control system design, only the first structural mode was modelled. This is equivalent to assuming that information about the three remaining structural modes were unavailable for the design process. These modes will, however, be included in the vehicle model used in the computer simulation to be presented. Second, the pitch-rate sensor was placed at the anti-node of the first structural mode.

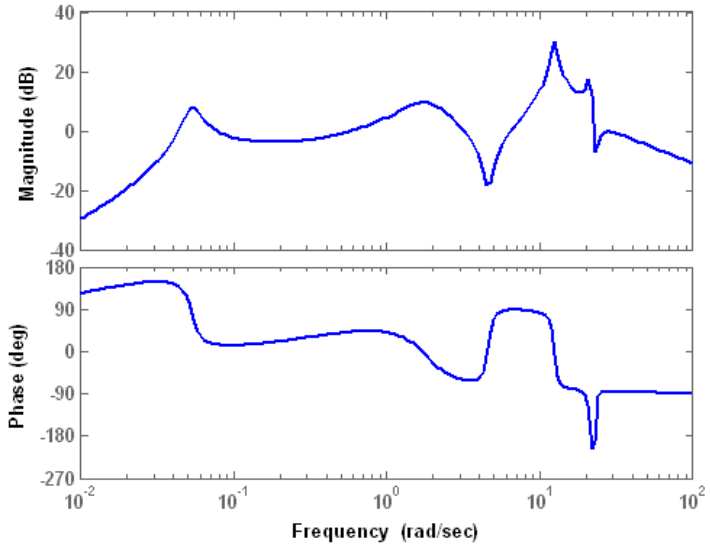

Figure 9 Bode plot of $q_{cp}(s)/\ )/\delta_{st}(s)$ (1/sec) for the unaugmented aircraft

The SMC design steps in Section 3 were followed as described below.

(1) The vehicle and actuator models have been obtained. The actuators were amplitude and rate-limited.

(2) A SISO pitch-rate control system is to be designed.

(3) The sliding manifold is selected as

$$\sigma = e(t) + 22\int e(t)dt \tag{19}$$

(4) Sliding behaviour was validated in a computer simulation with

$$u(s) = 3.72\sigma(s) \tag{20}$$

The open-loop crossover frequency was found to be approximately 45 rad/sec

(5) A boundary layer was created with $\varepsilon = 1.0$

(6) When actuator dynamics were included, the system was unstable.

(7) An asymptotic observer was created. The six observer eigenvalues were selected as

$$\lambda_i \ (i = 1,\ldots 6) = -5, -5.5, -6, -6.5, -7, -7.5 \text{ rad/sec} \tag{21}$$

When an 'equivalent' unity feedback loop transmission $L_{eq}(s)$ was created as

$$L_{eq} = \frac{q_{cp}/q_c}{1 - q_{cp}/q_c} \tag{22}$$

a crossover frequency of 6.82 rad/sec was found with an infinite gain margin and 77 deg phase margin. The reader is reminded that these calculations were done without the actuator in place. Also note that the original 45 rad/sec crossover frequency of the SMC system without the observer has been reduced considerably. The Bode diagram of $L_{eq}(s)$ is shown in Fig. 10.

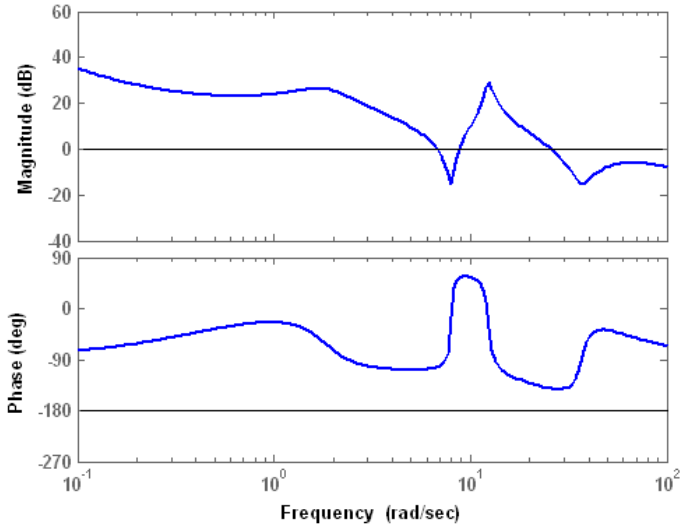

Figure 10 Bode diagram of $L_{eq}(s)$ for observer eigenvalue selection

(8) Hedge dynamics were created as

$$G_{hedge}(s) = \frac{121.4 \cdot s}{s^3 + 90s^2 + 2400s + 20000} \tag{23}$$

The Bode diagram of Fig. 9 demonstrates how the hedge gain was selected as described in Step (8) of Section 3. As opposed to Fig. 8, actuator dynamics were included in obtaining Fig. 11.

(9) Since only a single flight condition is being considered, no scheduling was undertaken.

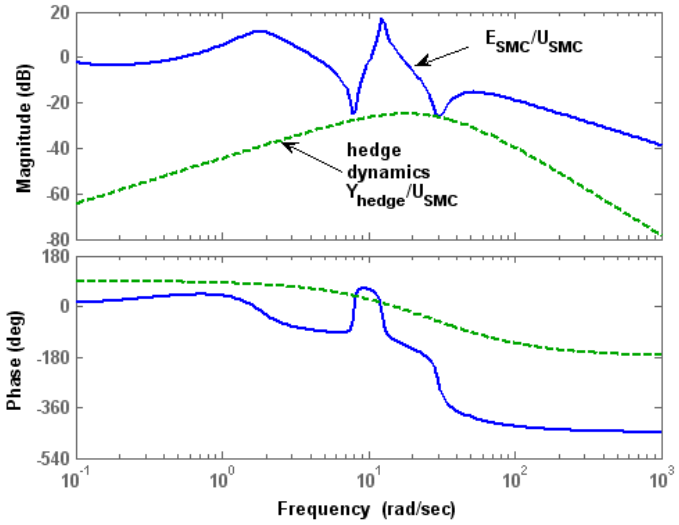

Figure 11 Selecting gain on hedge dynamics

In a preliminary computer simulation evaluation of the design just completed the system was found to be sensitive to computational and sensor delays. The observer, itself could not accommodate the significant non-minimum phase dynamics introduced by the delays (recall Step 2 of the Design Process of Section 3). To add robustness, an additional pitch-acceleration loop was closed around the final pitch-rate command system. Finally, an attitude command/attitude hold system response type was created. This is shown in Fig. 12 where

$$G = \frac{0.05s}{0.002s + 1} \qquad K = 2.25 \tag{24}$$

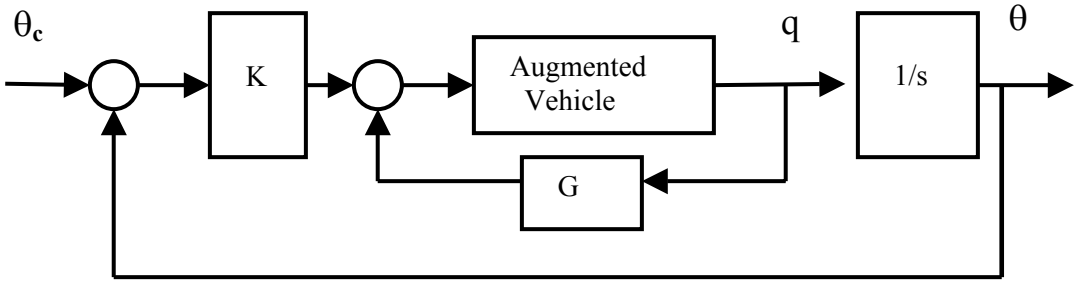

Figure 12 Modified feedback structure

5.1.2 Task-Independent Handling Qualities

Handling qualities were estimated using the technique discussed in Section 4. The Handling Qualities Sensitivity Function (HQSF) was calculated as given in Eq. 17. With the pilot/vehicle open-loop transfer function crossover frequency set to 2 rad/sec, the HQSF is plotted and is shown in Fig. 13, where it is seen that the HQSF violates the Level 1 bounds in the figure, thus predicting Level 2, "task independent" handling qualities.

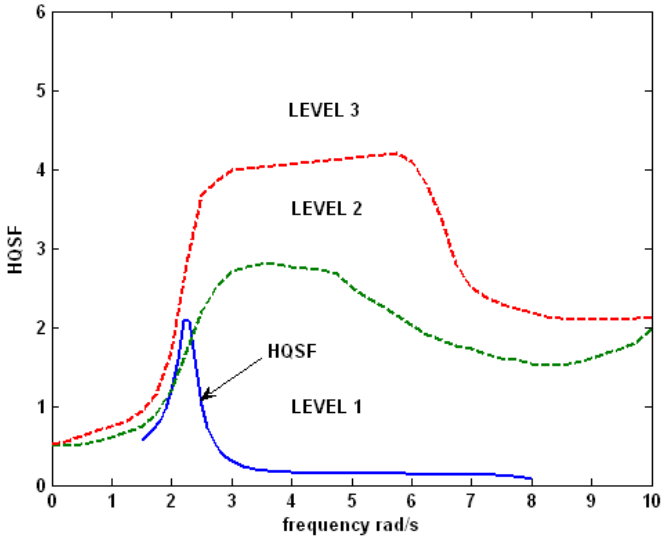

Figure 13 HQSF for pilot/vehicle system showing Level 2 handling qualities prediction

The failure of the design to achieve predicted Level 1 handling qualities can be attributed to the use of only a single control effector in the pitch-attitude system. An improved design approach would incorporate the small control vane near the cockpit (see Fig. 7) as a device dedicated to the suppression of aeroelastic effects sensed at the cockpit. Unfortunately, aerodynamic data for the vane was not available from [23].

5.1.3 Pilot/Vehicle Computer Simulation

A computer simulation of the pilot/vehicle system just created was undertaken. In this simulation, the complete 12 state vehicle model was utilized. In the simulation, sensor noise associated with the rate gyro was included and modelled as white noise passed through a second order filter with a 10 rad/sec bandwidth. The root-mean-square (RMS) value of the sensor noise was 0.25 deg/sec. Atmospheric turbulence disturbances (u_g, α_g and q_g) were included. The turbulence disturbances were again modelled as white noise passed through second order filters with 10 rad/sec bandwidths. The RMS values of the turbulence signals were 5 ft/sec for u_g, 0.435 deg for α_g (equivalent to 5 ft/sec w_g) and 4.32 deg/sec (equivalent to $-\dot{w}_g / U_0$). Finally, a time delay of 0.01 sec was included just before the actuator dynamics (modelling computational delay) and a delay of 0.01 sec was included just before the sensor noise was added (modelling sensor delay). The flight control task presented to the pilot was tracking as series of pulsive pitch attitude commands of ± 5 deg, with each pulse lasting 10 sec. Finally, a 'failure' is simulated 15 sec into a 50 sec simulation run by reducing the effectiveness of the stabilator by 75% (modelled as an instantaneous 75% reduction in the magnitude of the

signal being sent to the actuator) and by introducing an additional 0.025 sec time delay before the actuator. Figure 14 shows the pilot/vehicle tracking results. The pilot model is tracking with a 1.0 rad/sec crossover frequency. This value is commensurate with pilot/vehicle crossover frequencies that have been measured in flight tasks [25], [26]. Figure 15 shows the pilot model control inceptor inputs (δ_p) for this task. Finally, Fig. 16 shows the stabilator activity for the task. As in previous applications of the pseudo-sliding mode technique, control activity is the price to be paid for the system robustness. Increases in the magnitude of the computational or sensor time delays aggravated the high-frequency activity.

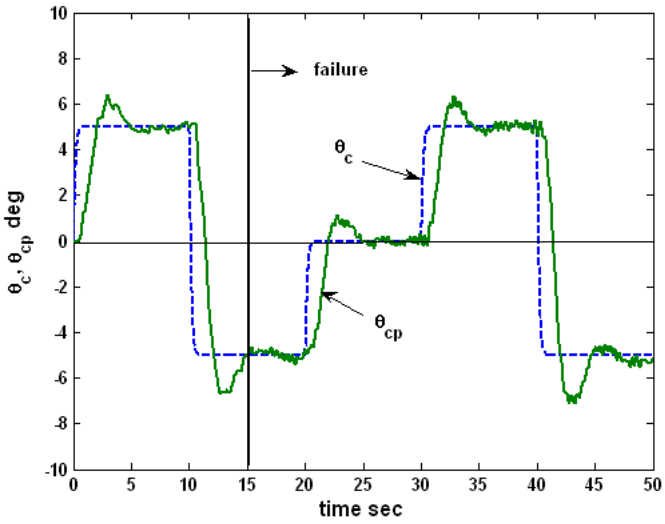

Figure 14 Computer simulation results for pilot/vehicle pitch-attitude tracking task

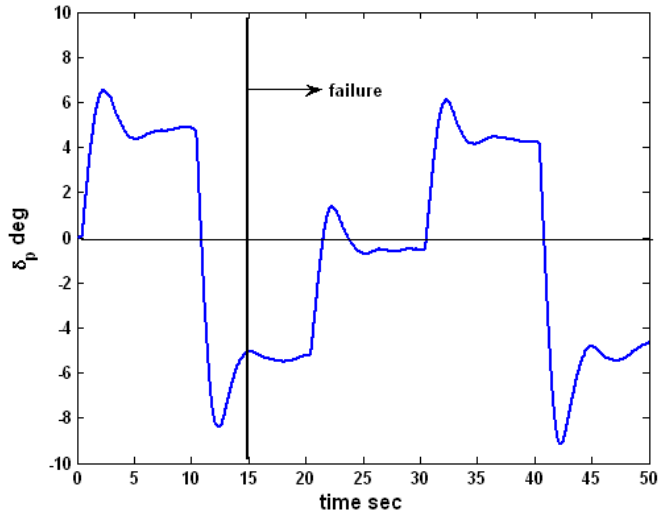

Figure 15 Pilot model control inceptor inputs for task of Fig. 14

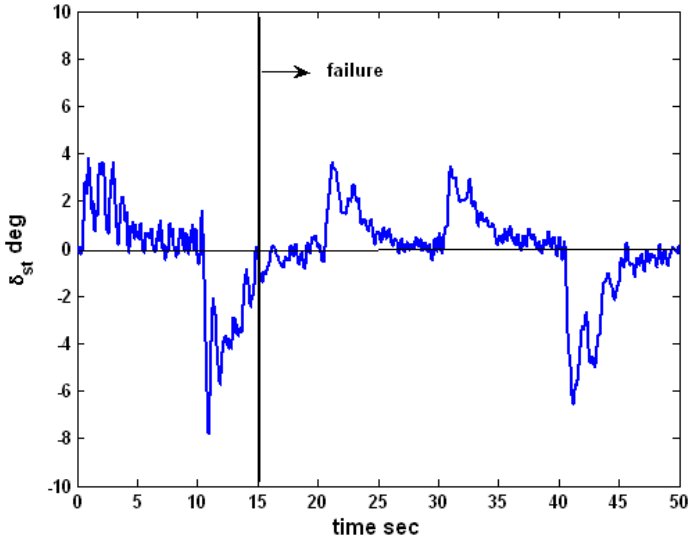

Figure 16 Stabilator activity for the task of Fig. 14

5.2 A Longitudinal and Lateral Flight Control System for an Innovative Control Effector (ICE) Vehicle

5.2.1 The SMC Design

The aircraft that is the subject of this example is shown in Fig. 17. The vehicle represents a conceptual low-observable fighter aircraft with a number of control effectors. Details of the vehicle model and the design procedure to be discussed can be found in [27]. Permission to reproduce figures has been granted by the Council of the Institution of Mechanical Engineers.

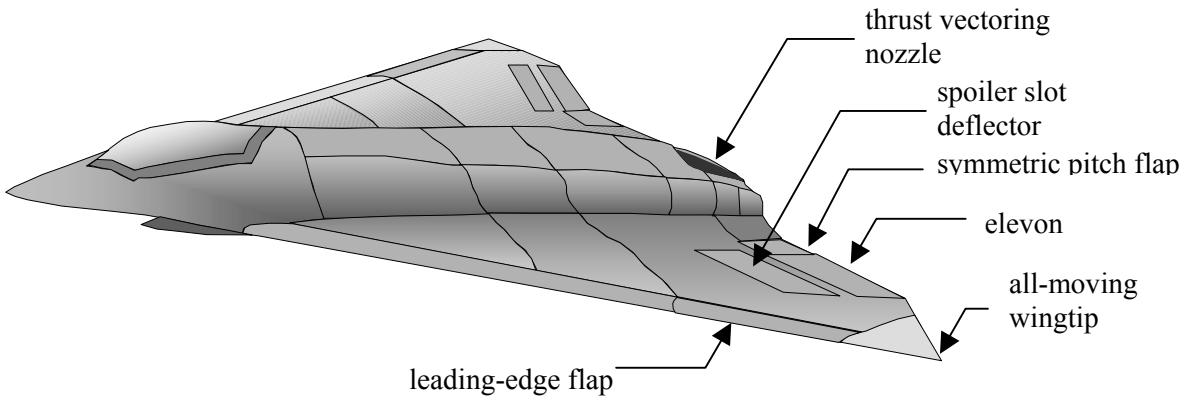

Figure 17 The ICE vehicle from [27]

The primary reasons for choosing this example were the multi-axis nature of the design, the fact that the unaugmented vehicle is unstable, multiple control effectors were involved, and a number of challenging

control actuator/effector failures could be simulated to demonstrate the robustness of the resulting design.

The SMC design steps in Section 3 were followed as described below.

(1) The vehicle and actuator models have been obtained. The actuators (11 in number) were amplitude and rate-limited.

(2) A MIMO control system is to be designed. This included a pitch-rate command, roll-rate command and side-slip command system. For convenience, the pitch-rate command system was created by first designing an angle of attack-command system, then placing a control shaping filter immediately after the pilot's longitudinal control input to provide a pitch-rate command system. Since three pseudo-control variables must be distributed to 11 control effectors, a control distribution matrix was needed. This 11 x 2 matrix was created using a pseudo-inverse design technique [28].

(3) Sliding manifolds were selected for each of the control axes. The resulting controllers are given by

$$\alpha\text{-loop:} \quad \frac{u_\alpha(s)}{\alpha_e} = \frac{5000(s+10)}{s}$$

$$\text{p-loop:} \quad \frac{u_p}{p_{s_e}}(s) = \frac{1000(s+10)}{s} \tag{25}$$

$$\beta\text{-loop:} \quad \frac{u_\beta}{\beta_e}(s) = \frac{5000(s+10)}{s}$$

The angle of attack control shaping filter was given by (0.2s+1)/(s+1).

(4) Sliding behaviour was confirmed in computer simulation

(5) Unity boundary layers were created for each of the control channels.

(6) The inclusion of actuator dynamics destabilized the controllers.

(7) Three asymptotic observers were created for each of the control channels. The observer eigenvalues

(eight for each loop) were selected as:

α-loop: λ = -1, -1.1, -1.2…,-1.7 rad/sec

p=loop: λ = -10, -10.1, -10.2…,-10.7 rad/s (26)

β-loop: λ = -0.5, -0.51, -0.52…,-0.57 rad/s

(8) Hedge dynamics were created for each control loop.

The dynamics for each loop were selected as:

$$\alpha\text{-loop:}\quad \frac{4s}{s^2+4s+1}$$

$$\text{p-loop:}\quad \frac{s}{s^2+4s+1} \tag{27}$$

$$\beta\text{-loop:}\quad \frac{4s}{s^2+4s+1}$$

(9) Although two different flight conditions were to be simulated (Mach No. = 0.3, Alt.= 15,000 ft and Mach No. = 0.9, Alt = 35,000 ft) the SMC controller was designed using the vehicle dynamics for the lower Mach No. and altitude. That is, no scheduling of the observer was considered. This was a deliberate decision made to evaluate the robustness of the design.

5.2.2 Task-Independent Handling Qualities

Pilot models for the pitch and roll-attitude loops were created as described in Section 4. No active sideslip control by the pilot was considered, i.e., the pilot was assumed to be flying with "feet on the floor." As an alternative to the HQSF, bandwidth-phase delay was used to assess the vehicle handling qualities [29]. Figure 18 shows the definitions of bandwidth and Fig. 19 defines the bounds used to determine handling qualities levels for this application. In Fig. 18, bandwidth, ω_{BW} is defined as the lesser of $\omega_{BW\ gain}$ and $\omega_{BW\ phase}$. Phase

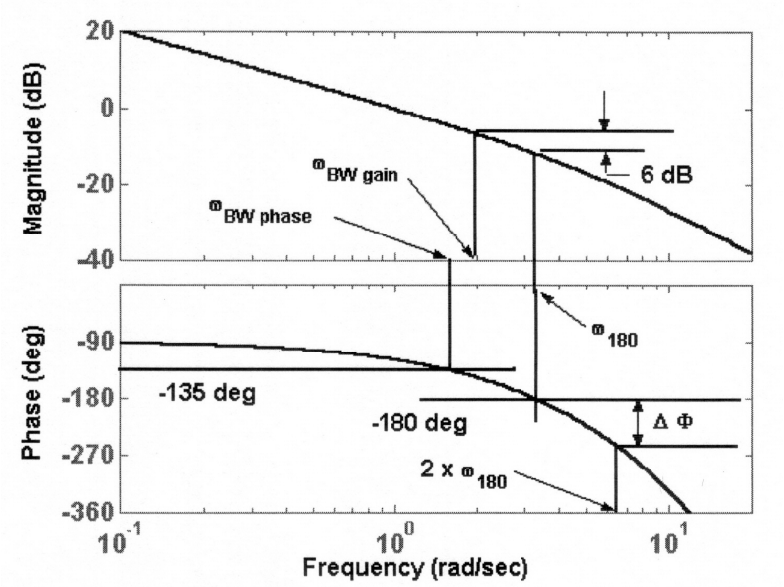

Figure 18 Determining bandwidth for handling qualities from [27]

delay is determined from Fig. 18 as

$$\tau_p = \frac{\Delta\Phi}{57.3(2 \text{ x } \omega_{180})} \tag{28}$$

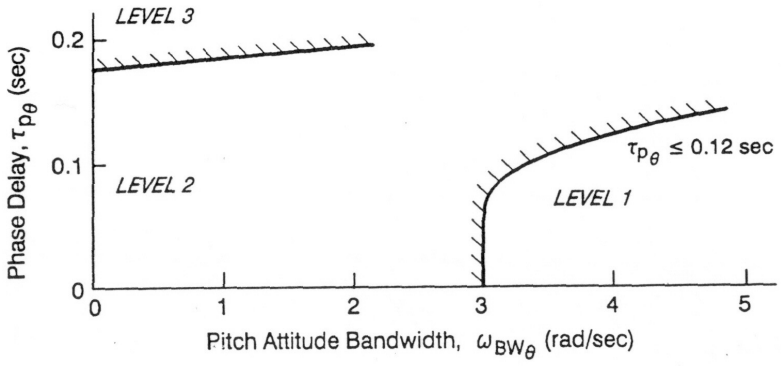

Figure 19 Boundaries for handling qualities levels for the pitch axis using bandwidth-phase delay from [27]

In using Fig. 19, for the roll axis, the bandwidth determined from Fig. 17 will be at last 1 rad/sec for Level 1. The phase delay will be nor more that 0.14 sec for Level 1 and no more than 0.2 sec for Level 2. Table 2 shows the results of the handling qualities analysis. Note that both flight conditions are considered.

Table 2 Bandwidth/Phase-Delay Results

	Mach No. = 0.3, Alt. = 15,000 ft		Mach No. = 0.9, Alt. = 35,000 ft	
	Pitch	Roll	Pitch	Roll
$\omega_{BW_{phase}}$ (rad/sec)	3.69	2.37	3.7	2.3
τ_p (sec)	0.07	0.1	0.07	0.11

5.2.3 Pilot/Vehicle Computer Simulation

The piloting tasks consisted of the pilot following a series of simultaneous pitch and roll-attitude commands for a period of 50 sec in each flight condition. The commands consist of a series of filtered pulses, alternating in sign. The amplitude of the pulses depends upon the flight condition and the command, i.e., whether it is a pitch or roll command. In comparing the command input to the corresponding pilot/vehicle response, a 1.0 sec delay is added to the recorded command signal. This delay accommodates the accumulative time delays in the pilot response and is only included for the purposes of performance assessment. The delay is not included in the input to the pilot/vehicle system in the simulation.

Mach No. = 0.3 Altitude = 15,000 ft θ_{amp} = 5 deg; ϕ_{amp} = 30 deg (29)

Mach No. = 0.9 Altitude = 35,000 ft θ_{amp} = 0 deg; ϕ_{amp} = 5 deg

It was assumed that all of the output variables to be specified for the linear vehicle models will be available for feedback in the control system design. These include airspeed perturbation, v, angle of attack, α, body pitch rate, q_b, pitch attitude, θ, sideslip angle, β, roll-rate about the x stability axis, p_s, yaw rate about the z stability axis, r_s, roll attitude, ϕ, and linear accelerations $a_{x_{cg}}$, $a_{y_{cg}}$, and $a_{n_{cg}}$. No sensor dynamics were modelled with the exception of a 0.02 sec time delay assumed for each sensed variable. Additive sensor noise was included in each measured variable. Finally, a failure suite was considered in the computer simulation consisting of six, cumulative system failures of increasing severity as defined in Table 3.

Figures 20-25 show the pilot/vehicle tracking performance for the two flight conditions. Failure 6 from Table 3 is introduced at t = 20 sec. Recall that the SMC design was based entirely on the vehicle dynamics of the first flight condition, i.e., Mach No.= 0.3 and Alt =15,000 ft. Finally, Fig. 26 shows the effect of sensor noise on one of the control effector inputs. Again, one sees that control activity is the price to be paid for the robustness demonstrated in Figs. 20-25.

Table 3 System Failures

Failure	Failure Description
1	Left elevon actuator amplitude limits reduced to ±15 deg; rate limits to ±15 deg/sec
2	Failure 1 plus symmetric pitch flap actuator with hard-over of + 5 deg
3	Failures 1-2 plus left spoiler actuator with rate limits reduced to
4	Failures 1-3 plus left leading-edge outboard flap with hard-over of + 5 deg
5	Failures 1-4 plus pitch nozzle actuator with rate limits reduced to ±10 deg/sec
6	Failures 1-5 plus elements of the unuaugmented plant **A** and **B** matrices each change by ±20 percent (excluding kinematic terms)

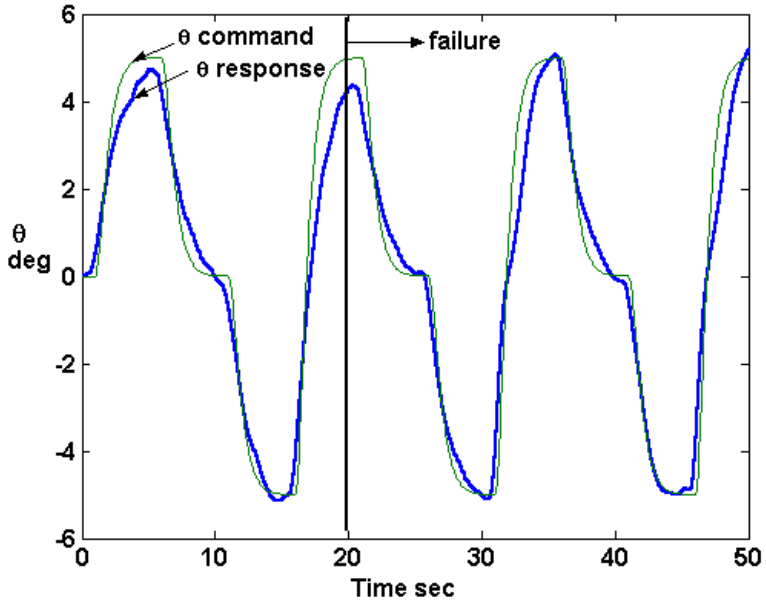

Figure 20 Pitch-attitude tracking, Mach No. = 0.3, Alt. = 15,000 ft from [27]

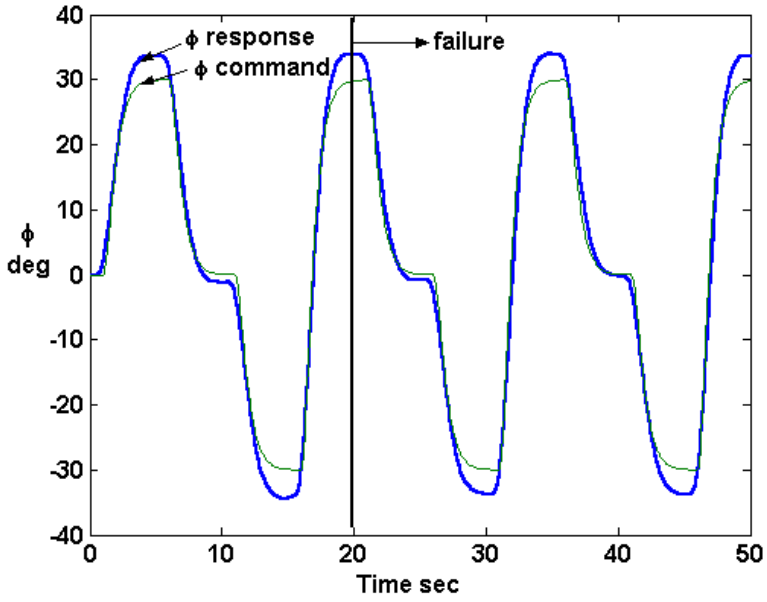

Figure 21 Roll-attitude tracking, Mach No. = 0.3, Alt. = 15,000 ft from [27]

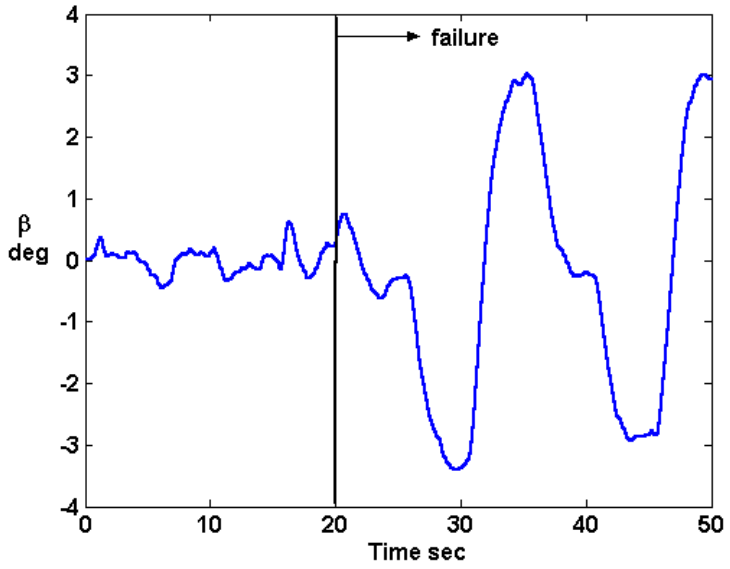

Figure 22 Sideslip regulation, Mach No. = 0.3, Alt. = 15,000 ft from [27]

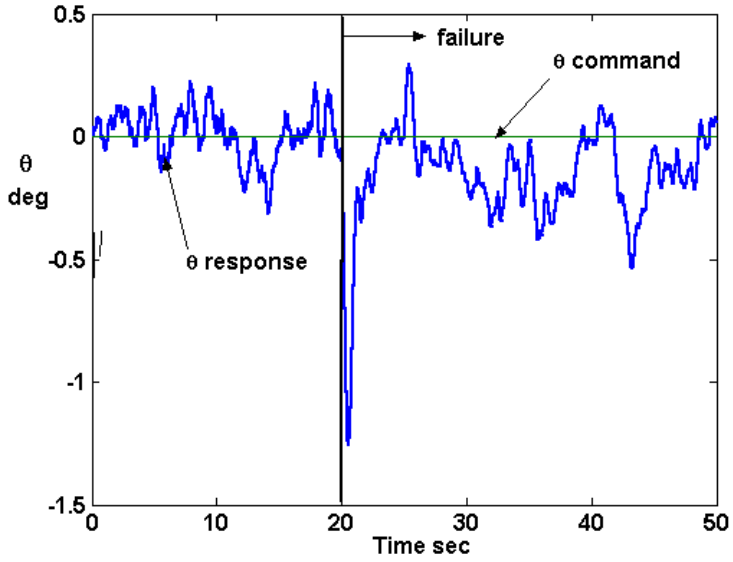

Figure 23 Pitch-attitude regulation, Mach No. = 0.9, Alt. = 35,000 ft from [27]

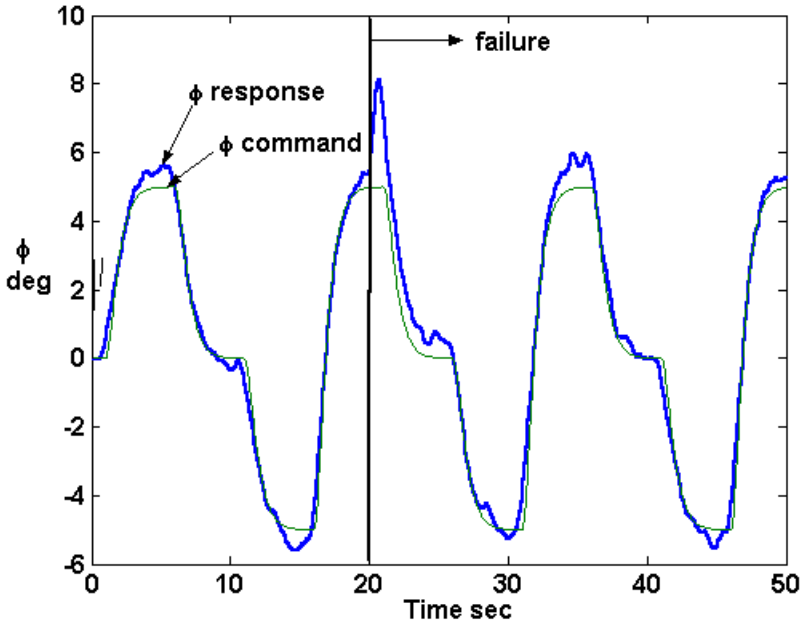

Figure 24 Roll-attitude tracking, Mach No. = 0.9, Alt = 35,000 ft from [27]

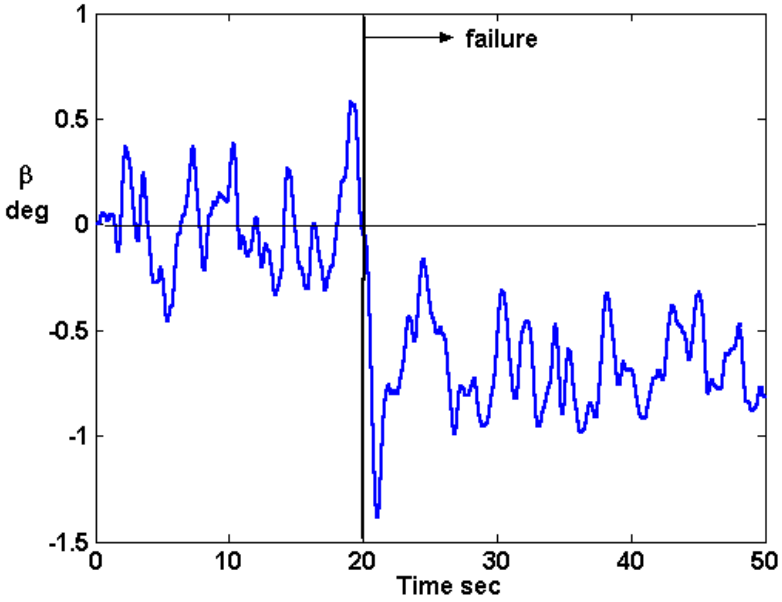

Figure 25 Sideslip regulation, Mach No. = 0.9, Alt. = 35,000 ft from [27]

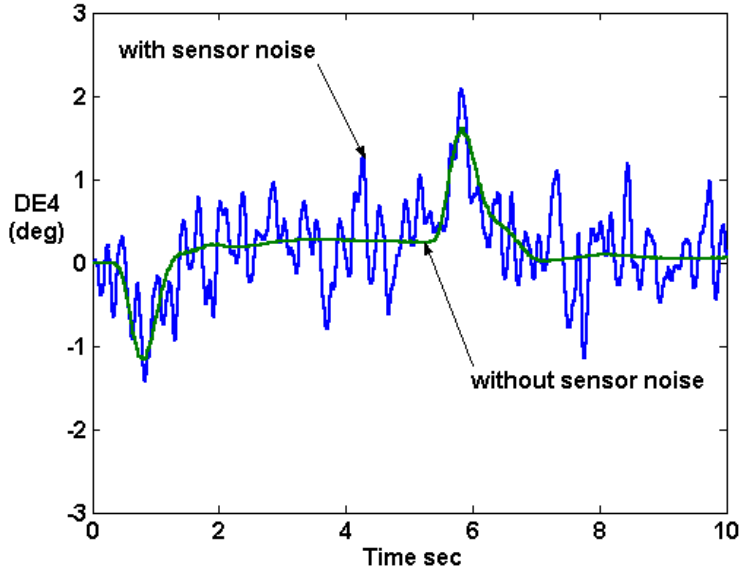

Figure 26 Symmetric pitch flap inputs, Mach No. = 0.3, Alt. = 15,000 ft showing effect of sensor noise from [27]

5.3 Control of a Nonlinear Model of a 21-Inch Ducted-Fan UAV

5.3.1 The SMC Design

The vehicle that is the subject of this example is a ducted fan UAV and is shown in Fig. 27. The diameter of the duct is 29 inches. The vehicle has actuator-driven vanes within the duct in the downwash of the vehicle's propeller. These vanes, shown in Fig. 28 control vehicle pitch, roll, and yaw with variable engine RPM controlling thrust. Four actuators mounted inside the duct actuate the control vanes. A body-fixed "helicopter" axis system is employed in this study, with the z-body axis directed downward and coincident with the rotor axis. The vane sets are deflected collectively or differentially to create moments about each of the body axes. Models of amplitude and rate-limited actuators are included for pitch, roll and yaw control. A simple engine model is included consisting of a first-order lag with a 0.25 sec time constant. This example differs from those of Sections 5.2 and 5.2 in that the vehicle model is highly nonlinear function of flight condition. Details of the design procedure can be found in [30].

Figure 27 A 29-inch UAV

The SMC design steps in Section 3 were followed as described below.

(1) The vehicle and actuator models have been obtained. The actuators were amplitude and rate-limited. The model is identical to that used in [31].

(2) A MIMO control system is to be designed. The control distribution matrix was the identity matrix. The control architecture was created with the structure shown in Fig. 29. Here, the earth-fixed velocity components U, V, W are transformed to body-fixed velocity components u, v, and w. Then the x-body axis velocity component u is controlled through pitch-attitude θ, which, in turn is controlled through pitch-rate q, finally controlled through δ_{pitch}, deflection of the pitch-vane system. The y-body axis velocity component v is controlled through roll-attitude ϕ, which, in turn is controlled through roll-rate p, finally controlled through δ_{roll}, the deflection of the roll-vane system. Yaw attitude ψ receives no outer-loop command and is controlled through yaw-rate r that is finally controlled δ_{yaw}, the deflection of the yaw-vane system. Finally, the z-body axis velocity component w is controlled through δ_{rpm}, the engine RPM. Only the variables within the box in Fig. 28 are involved directly with the SMC design. The SMC design was based upon the vehicle dynamics at hover.

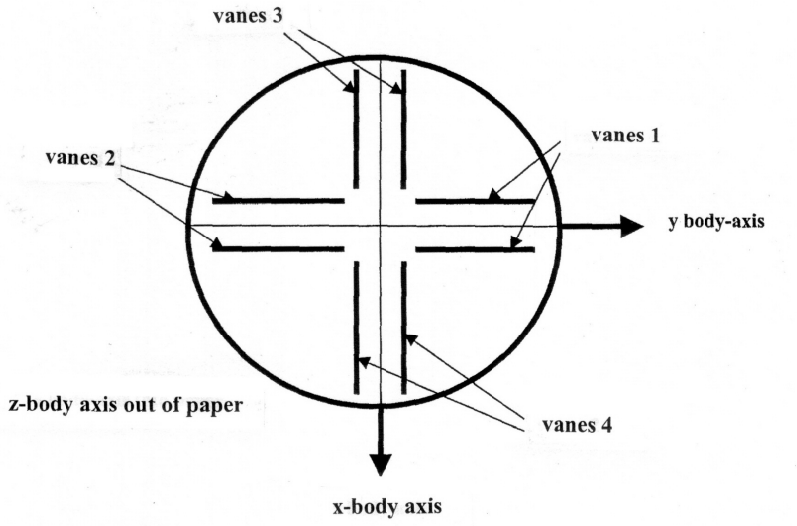

Figure 28 Vane arrangement for UAV (viewed from beneath)

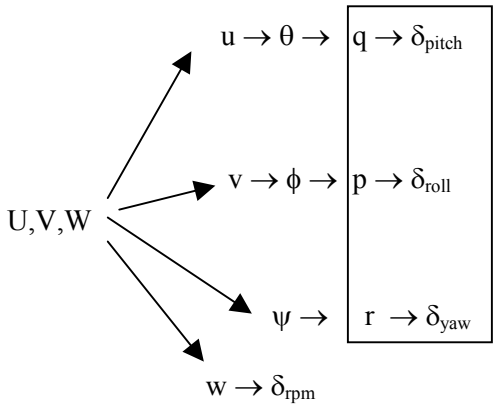

Figure 29 Control architecture

(3) Sliding manifolds were created for each of the control axes. The resulting controllers are given by:

$$u(s) = \rho\left[1 + \frac{2}{s}\right]e(s) \tag{30}$$

where, for the inner, attitude-rate loops, $\rho_q = 90$, $\rho_p = 150$, $\rho_r = 75$.

(4) Sliding behaviour was validated in a computer simulation with the system of Eq. 30. The crossover

frequencies for each loop were 50 rad/sec.

(5) A boundary layer was implemented with unity thickness, eliminating the infinite-frequency switching.

(6) The system was unstable when actuator dynamics were included.

(7) A single asymptotic observer was created to service each of the attitude-rate SMC channels. The measured variables were attitude rates p, q, and r, attitudes, ϕ, θ, and ψ, and body-axis velocity components u, v, and w. These variables were chosen as they are identical to those used in [31]. Figure 30 compares the effective unity-feedback loop transmissions for the pitch-rate loop for observer eigenvalues of λ = -1, -5, -10 and –20 rad/sec. Each eigenvalue set contains nine eigenvalues corresponding to the number of states in the vehicle model without actuators.

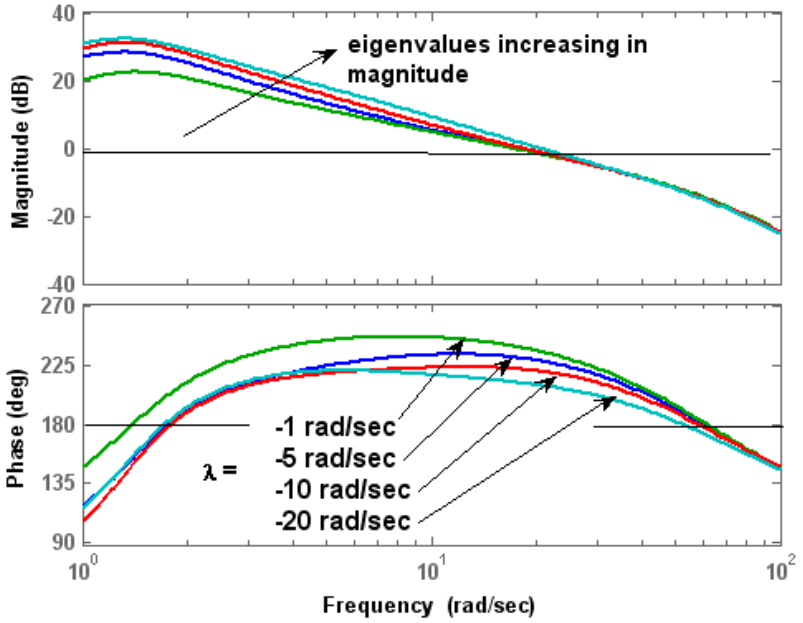

Figure 30 Equivalent unity-feedback loop transmissions for pitch-rate control loop showing effect of observer eigenvalue selection

The magnitude and phase characteristics evident in Fig. 30 led to the selection of observer eigenvalues as –5 rad/sec. This selection was based upon a tradeoff between maximizing both low-frequency Bode magnitude and phase margin. Only those response variables required by the SMC system (p, q, r) were obtained from the observer. The resulting crossover-frequency for all attitude-rate loops is approximately 20 rad/sec. Attitude loops were closed with crossover frequencies of approximately 5.5 rad/sec. The outer body-axis velocity loops were closed with crossover frequencies of approximately 1.1 rad/sec. In each case, desirable K/s – like loop transmissions were in evidence around crossover, with ratios of crossover frequencies between successive loops of approximately 3.6 and 5.

(8) No reference model hedging was employed in the design. This added complexity was avoided since, as the

next step describes, the observer was scheduled with flight condition in the final design.

(9) The observer was scheduled with flight condition. It should be emphasized that this step was not necessary to provide stability over the envelope to be considered. Rather observer scheduling resulted in a significant reduction in control activity as compared to a design in which it was absent. The observer was scheduled with flight condition defined as steady, level flight at velocities from 0 (hover) to 50 ft/sec. The state-space vehicle model linearized about the six trim velocities of hover, 10, 20, 30,40 and 50 ft/sec was used in the observer, with linear interpolation of the matrix elements between flight conditions. Observer eigenvalues remained at the nominal –5 rad/sec value. Figure 31 shows the Bode plots for the q/u_{pitch} transfer functions for the six flight conditions and demonstrates the near invariance of the dynamics at frequencies near the inner-loop crossover frequency of 50 rad/sec (before observer implementation). The apparent phase disparity merely represents a 360 deg phase shift.

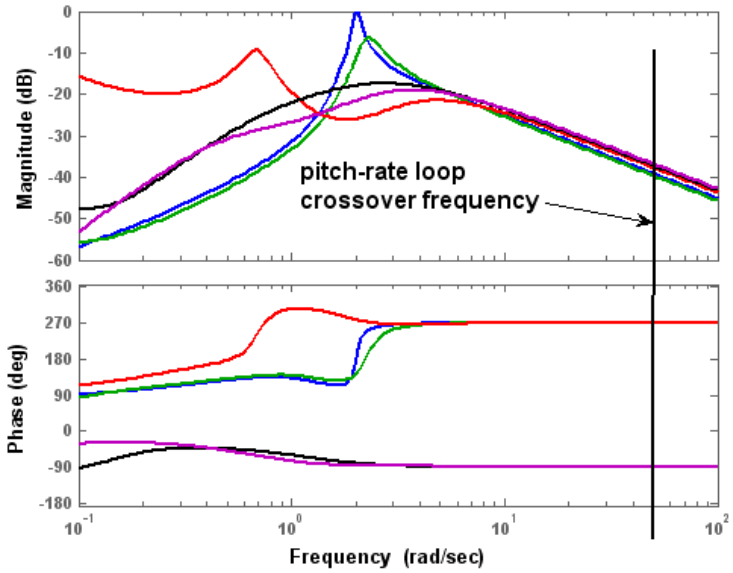

Figure 31 Bode plot of q/u_{pitch} transfer functions for six trim flight velocities

5.3.2 Computer Simulation

As opposed to the previous design examples, this application is intended to address autonomous control, and no pilot model or handling qualities assessment is undertaken. A representative flight profile was chosen as follows. The vehicle was to follow a velocity command (in an earth-fixed axis system) consisting of an acceleration from hover to a horizontal velocity of 50 ft/sec in 30 sec, steady flight at 50 ft/sec for 50 sec, then a deceleration to hover. There was a simultaneous short-duration velocity command in the vertical direction of approximately 18 ft/sec, and a return to hover.

To emphasize the variation in vehicle dynamics between hover and 50 ft/sec, Table 4 shows the percentage changes in selected elements of the **A** and **B** matrices of the linearized state-space description of the vehicle

between the two, trimmed flight conditions.

Table 4 Variation in Linear State Space Matrix Elements Between Hover and 50 ft/sec Flight Conditions

A,B matrix elements	% change from hover
A(5,1)	-195% (including sign change)
A(4,2)	+32%
A(1,1)	- 46%
A(1,3)	+988% (including sign change)
A(2,2)	-29%
A(3,3)	-94%
B(5,1)	+31%
B(4,2)	+32%
B(6,3)	-10%
B(3,1)	-20%

Atmospheric turbulence with root-mean-square (RMS) intensities of 5 ft/sec were included in the x, y and z earth-fixed axes. Sensor noise we included for each measured variable. These were 0.1 ft/sec for body-axis velocities and 0.1 deg/sec and 0.1 deg for attitude-rates and attitudes. In addition, to demonstrate the robustness of the design, unmodelled 0.01 sec time delays were included in each sensor loop and 25% unmodelled increases in the principal moments of inertia of the vehicle were included. Figure 32 shows the tracking performance, where Uc and Wc represent the inertial velocity commands. Fig. 33 shows the control vane and engine RPM time histories. Figure 34 shows the vehicle pitch attitude variation during the maneuver.

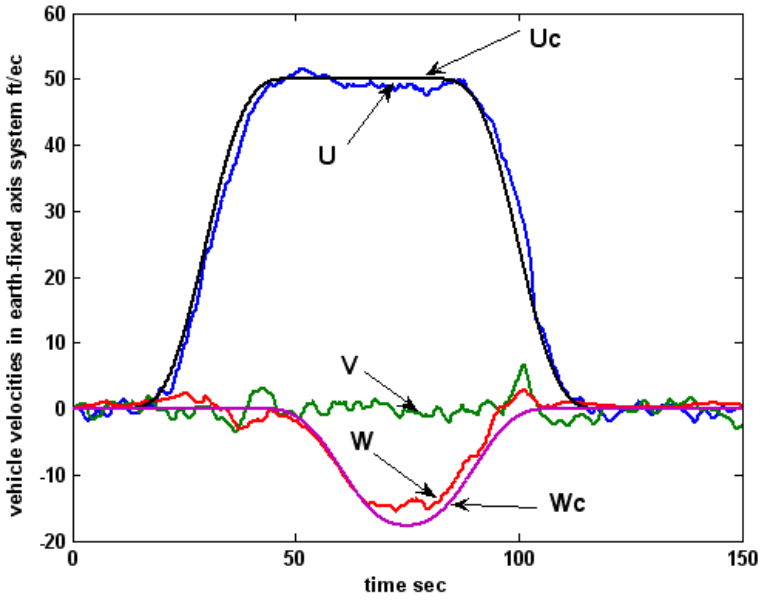

Figure 32 Vehicle inertial velocity commands and responses

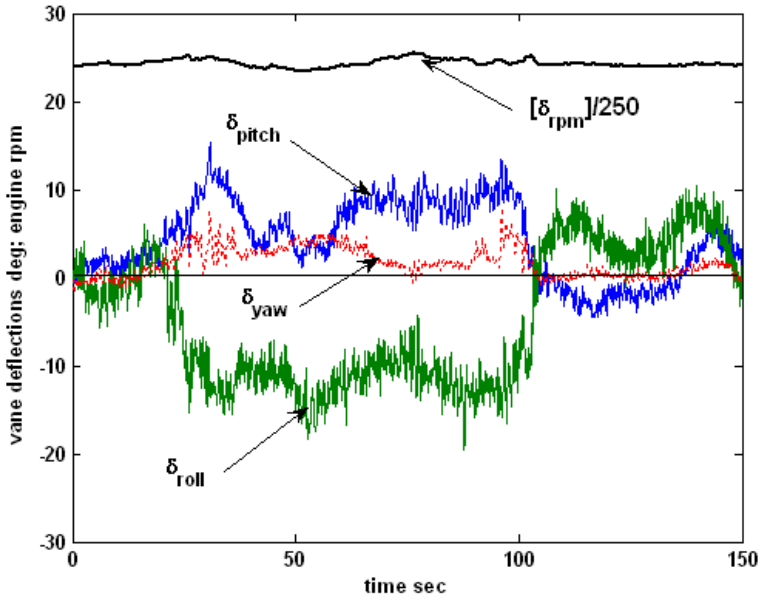

Figure 33 Vane deflections and engine RPN for responses of Fig. 30

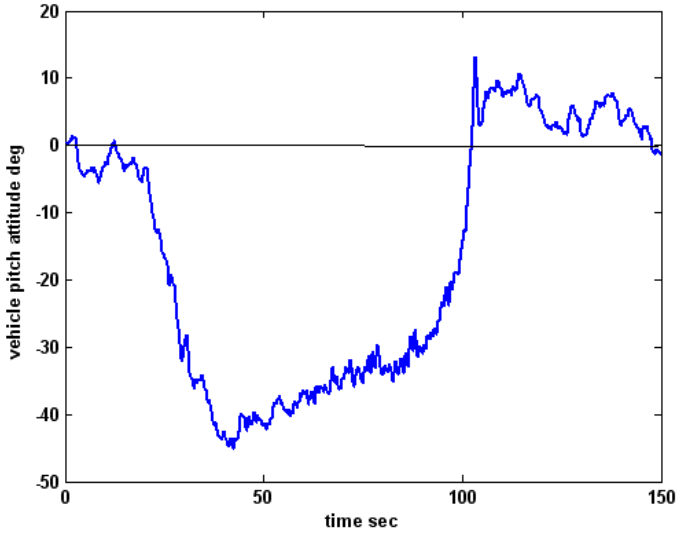

Figure 34 Vehicle pitch attitude for responses of Fig. 30

5.4 Control of a Nine-Inch Micro-Air Vehicle Model Near Hover

5.4.1 The SMC Design

The vehicle that is the subject of this example is shown in Figure 35. This vehicle is the smallest member of a class of UAVs that included the vehicle of Section 5.3. As opposed to the model of Section 5.3, the

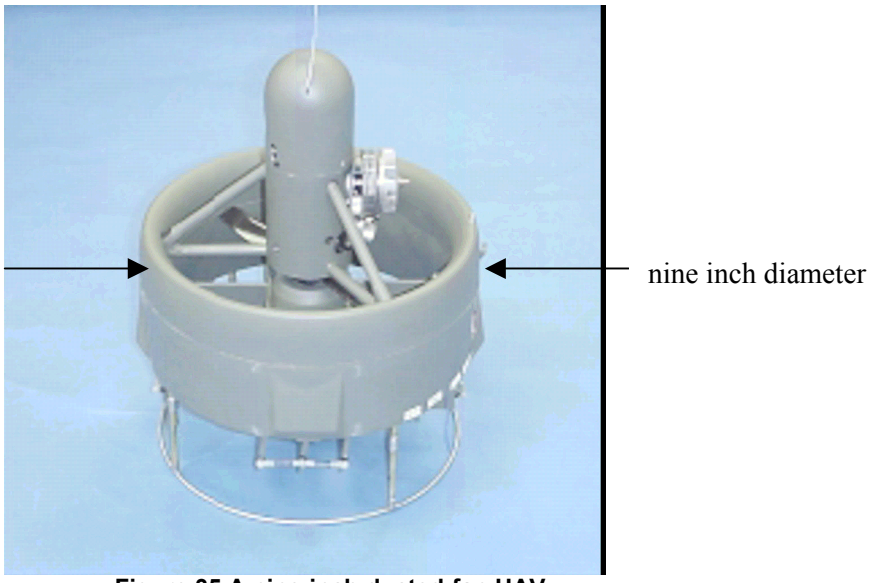

Figure 35 A nine-inch ducted-fan UAV

aerodynamic model used in this example is linear, and valid only for flight near hover. The reason for the inclusion of this example, is to demonstrate the capabilities of the proposed design technique for micro-air vehicles and to demonstrate the ability of the vehicle to maneuver autonomously in the presence of atmospheric disturbances. Details of the design procedure can be found in [32].

The SMC design steps in Section 3 were followed as described below.

(1) The vehicle and actuator models have been obtained.

(2) A MIMO pitch-rate, roll-rate, and yaw-rate, inner-loop control system is to be designed via the SMC technique. No control distribution matrix was required. It should be noted that the body axis system for this application differs from that of the 21-inch UAV of the previous section. Here the x-body axis is parallel to the propeller shaft. x-body axis velocity is controlled by engine RPM and the controller is not part of the SMC design due to its relatively low bandwidth. Outer attitude and position loops will be designed by classical-loop shaping techniques. The vane deflections δ_E, δ_A, and δ_R refer to deflections that give rise to moments about the x, y, and z, body-axes, respectively [31].

(3) The sliding manifolds for the SMC controller were chosen as:

$$u(s) = \rho\left[1 + \frac{5}{s}\right]e(s) \quad \text{(pitch rate and roll rate)} \tag{31}$$

$$u(s) = \rho\left[1 + \frac{10}{s}\right]e(s) \quad \text{(yaw rate)}$$

(4) Sliding behaviour was validated in a computer simulation with

$$\begin{aligned} \rho_q &= -80 \\ \rho_p &= -110 \\ \rho_r &= -100 \end{aligned} \tag{32}$$

The open-loop crossover frequencies were 100 rad/sec.

(5) Boundary layers were created with unity thickness.

(6) When actuator dynamics were included, the system was unstable.

(7) An asymptotic observer was created which served each of the three SMC channels, i.e. as opposed to the design for the 21-inch vehicle, separate observers for each channel were not designed. To permit a comparison with a competing design technique (the "gain optimized" of [33]), it was assumed that all vehicle states were available as inputs to the observer. The eigenvalues selection was based upon stability margins as revealed in the Bode plots of the effective, unity-feedback loop transmissions like that defined in Eq. 22. Figure 36 shows one such Bode plot. Table 5 is a typical stability margin comparison for the pitch-rate and roll-rate loops. The similarity between the pitch-rate and yaw-rate loops meant that the L_{eq} for the yaw-rate loop need not be

examined. The nine eigenvalues were

$$\lambda = -25, -25.05, -5.5 \ldots -25.4 \text{ rad / sec} \tag{33}$$

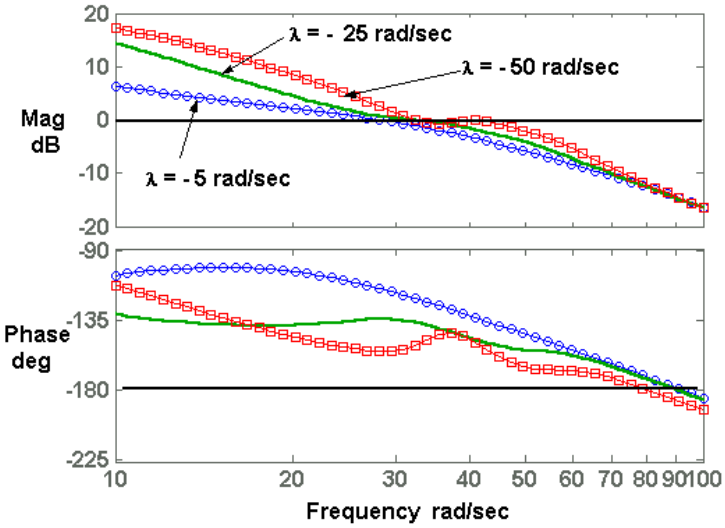

Figure 36 Comparison of equivalent, unity feedback loop transmissions for the pitch-rate loop for different eigenvalue sets from [32]

Table 5 Comparison of stability margins of equivalent loop transmissions

	λ = -25 rad/sec set		λ = -50 rad/sec set	
	pitch-rate	roll-rate	pitch-rate	roll-rate
Loop Transmission	L_{eq}	L_{eq}	L_q	L_p
Phase Margin	43 deg	47 deg	28 deg	44 deg
Gain Margin	15 dB	> 20 dB	12 dB	10.2 dB

(8) As in the example with the 21-inch UAV, reference model hedging was not employed in this design.

(9) Since only flight near hover is being considered, no scheduling of the observer was undertaken.

5.4.2 Computer Simulation

A simulation of the competing control designs was conducted. The task consisted of the vehicle starting from a stabilized hover at coordinates [0,0,0] ft. A series of waypoints were then commanded with the following coordinates: [80,0,20] ft, [160,40,0] ft, [80,-40,20] ft, and [0,0,0] ft. The control systems were analog in nature, however in the computer simulations, zero-order holds with a 0.01 sec sample interval (50 Hz sampling frequency) were inserted before each actuator to emulate a digital control law implementation. Figures 37 and 38 show vehicle trajectory in earth-fixed coordinates for the SMC system. Figure 39 shows the time histories of both the gain optimized design of [33] and the SMC design. Given the scales of Fig. 39, the time histories for the two systems are seen to be nearly identical. Figures 40-43 compare the vane and RPM time histories for the two designs. With the exception of the δ_{RPM} comparison of Fig. 43, the SMC design is seen to be exhibit a higher frequency content, especially for the δ_A comparison of Fig. 41. This result is to be expected since, as has been emphasized in previous examples, the SMC approach espoused herein produces relatively high-bandwidth systems.

To assess the robustness of the two design approaches, the vehicle dynamics were varied as follows: the non-kinematic elements of the vehicle A matrix were varied by ± 50% as were the elements of the vehicle B matrix. In addition, a ± 2 deg dead zone was now included in the feedforward path of each vane actuator model. This dead zone could represent damaged or badly worn actuators. Referring to Figs. 40-42, one sees that this ± 2 deg dead zone significantly exceeds the maximum vane rotations that occurred with the nominal vehicle.

The gain-optimized design did not remain stable in this configuration. Figure 44 shows the [x,y,z] performance of the SMC design. Figure 45 shows the δ_A time history for this system. The system performance in terms of vehicle position is comparable to that of the nominal vehicle, although considerably more control activity is in evidence than for the nominal vehicle.

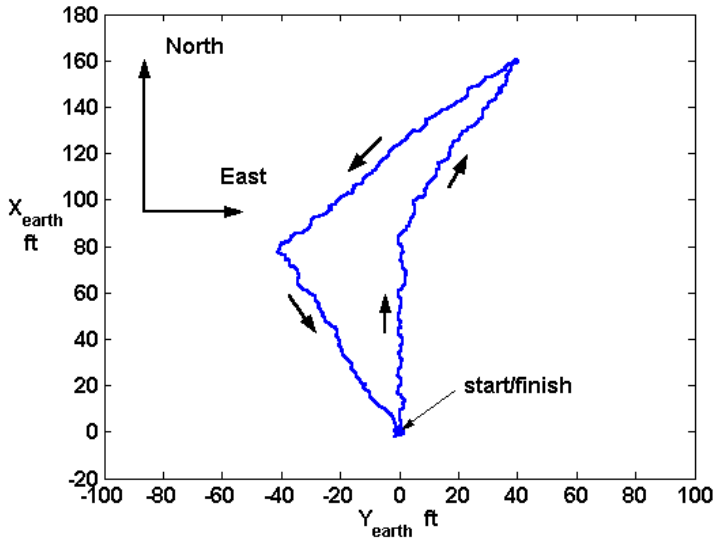

Figure 37 Vehicle trajectory in earth-fixed xy axes from [32]

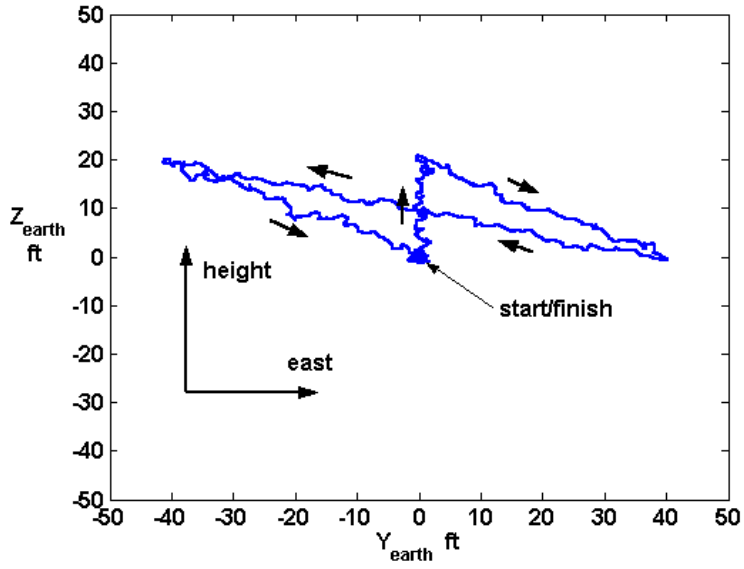

Figure 38 Vehicle trajectory in earth-fixed yz axes from [32]

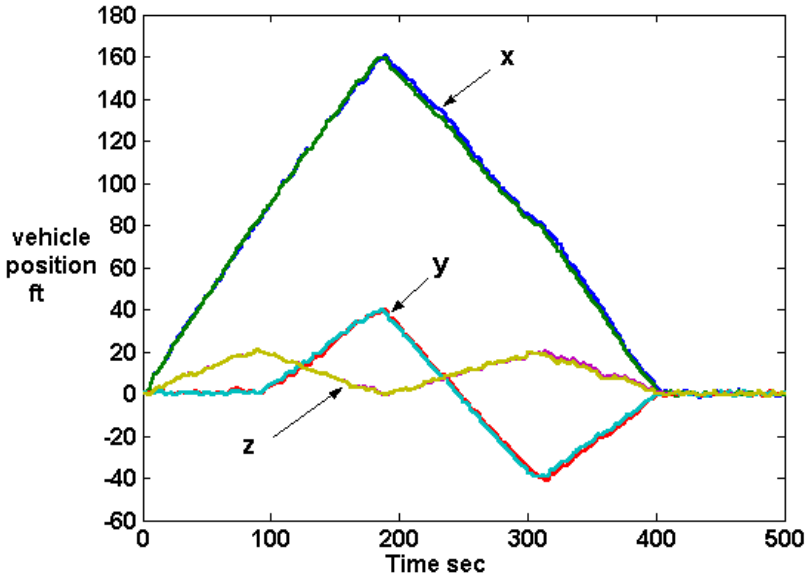

Figure 39 Vehicle position for gain optimized and SMC designs from [32]

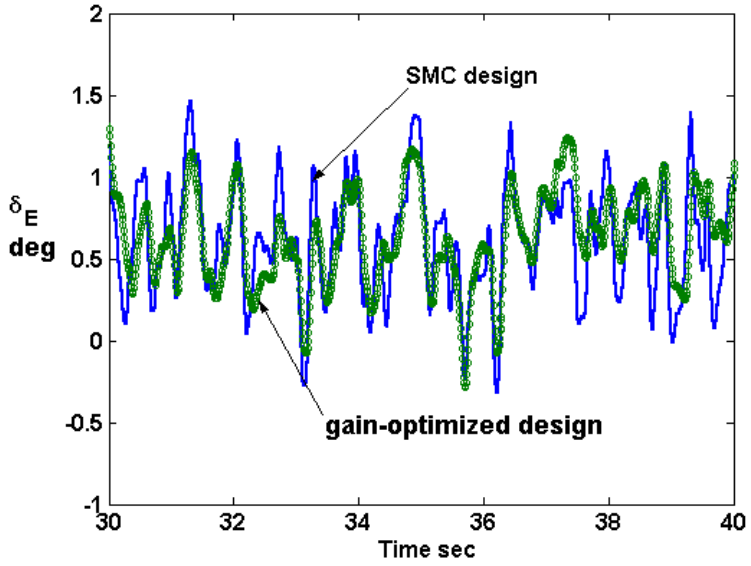

Figure 40 δ_E for gain-optimized and SMC designs from [32]

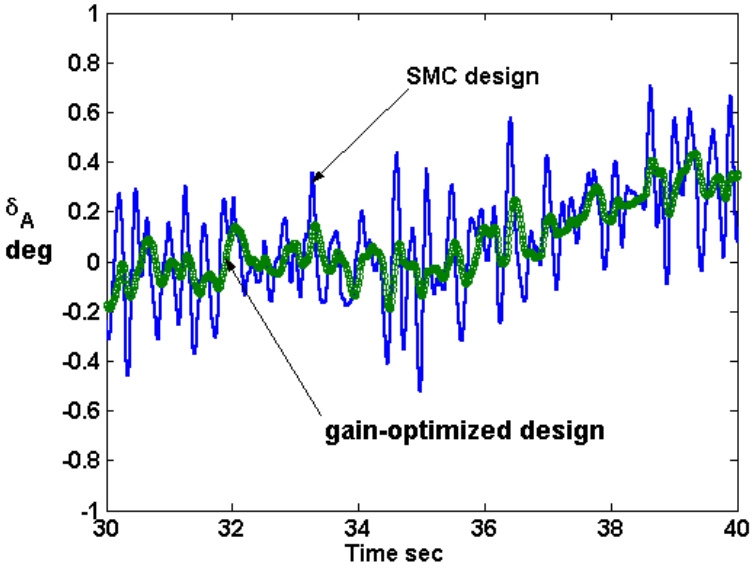

Figure 41 δ_A for gain-optimized and SMC designs from [32]

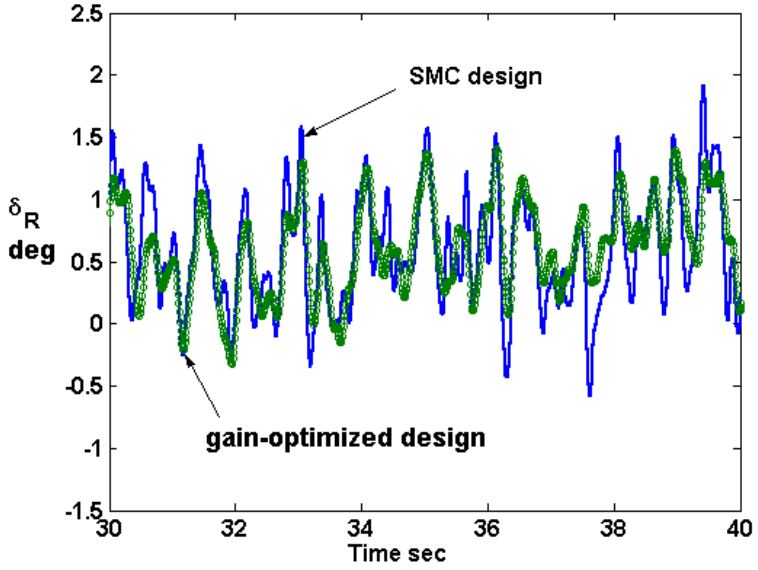

Figure 42 δ_R for gain-optimized and SMC designs from [32]

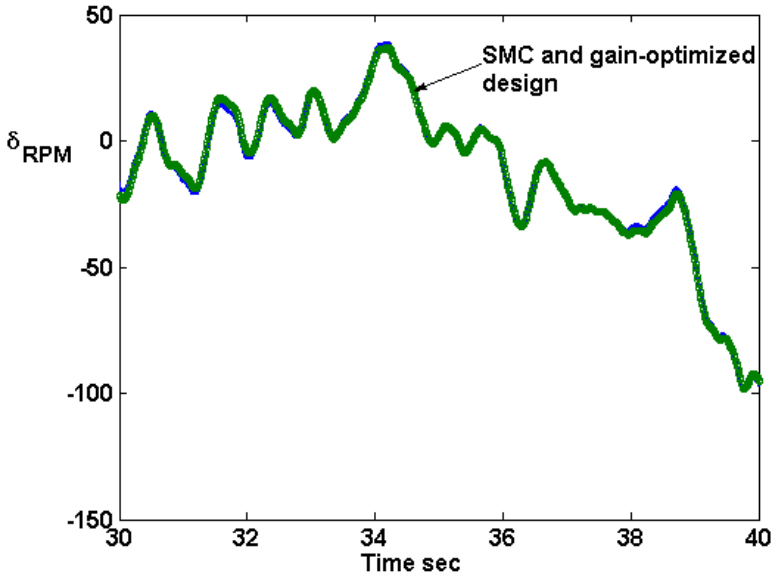

Figure 43 δ_{RPM} for gain-optimized and SMC designs from [32]

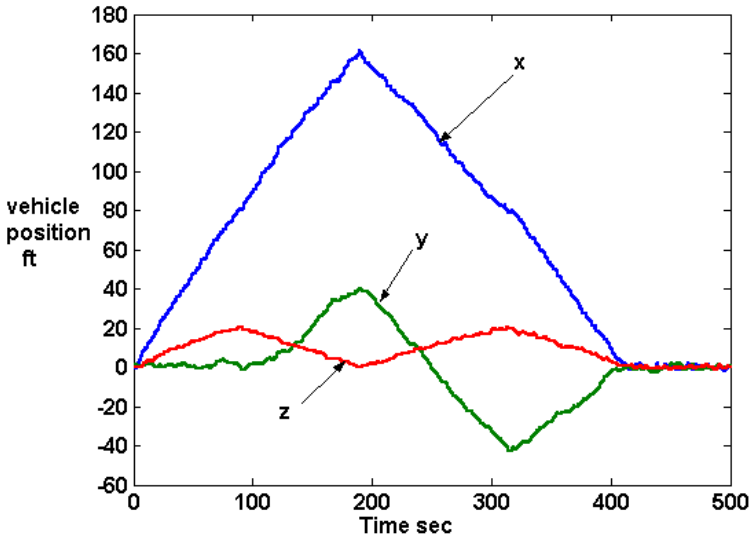

Figure 44 Vehicle position for SMC design with altered dynamics and vane actuator deadzone from [32]

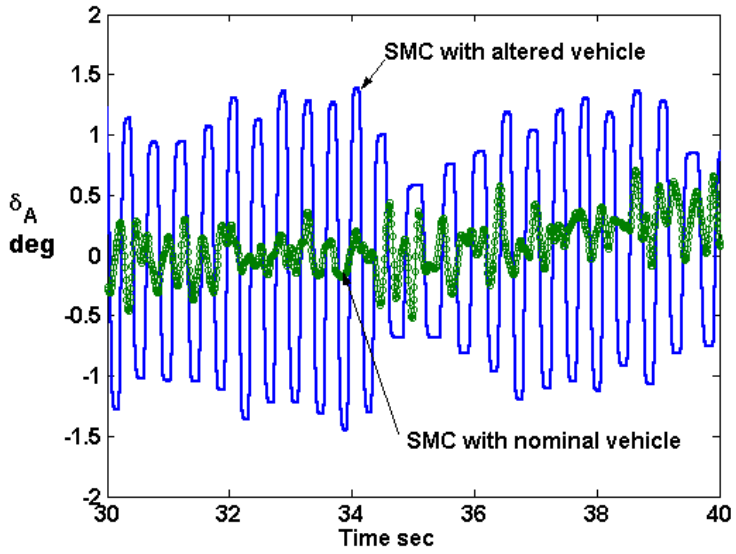

Figure 45 δ_A form SMC design, nominal vehicle and vehicle with altered dynamics and vane actuator deadzone from [32]

5.5 Control of a Notional Model of a Mesicopter

5.5.1 The SMC Design

Figure 46 shows a model of a so-called mesicopter UAV, a concept originating at Stanford University [34]. The vehicle shown weighs approximately 15 g (0.147 N)[1]. As such, it is borders on the size and weight of the vehicle class identified by DARPA as a "nano-scale" vehicle. The mesicopter is powered by four electric motors. The sense of the angular velocities of the rotors is indicated in Fig. 46. These angular velocities allow independent application of pitching moments, rolling moments, yawing moments and vertical thrust changes. Thrust on each rotor is varied through motor angular velocity. From Fig. 46 it is seen that diagonal pairs of rotors, e.g., rotors 1 and 3, spin in opposite directions. Pitch inputs are achieved by varying thrust on rotors 1 and 2 and roll inputs are achieved by varying thrust on rotors 3 and 4. Vertical thrust is achieved through simultaneous changes in thrust on all rotors. Finally, yaw inputs are achieved by increasing (decreasing) thrust on rotors 3 and 4 while decreasing (increasing) thrust on rotors 1 and 2. In this elementary analysis, only motion in the vertical plane is considered. The vehicle dynamics were created from fundamental principles. As in [35], rotor aerodynamic performance was derived using assumptions valid for full-scale rotorcraft. The author is aware of the limitations of these assumptions, and this vehicle model is offered only as an example of the synthesis procedure. The resulting nonlinear model was then linearized about a hover condition. This linear model was then used in both the control system synthesis and computer simulation. The linear model exhibited longitudinal dynamics representative of a hovering vehicle, i.e. an unstable "hovering cubic" and a stable heave mode [1].

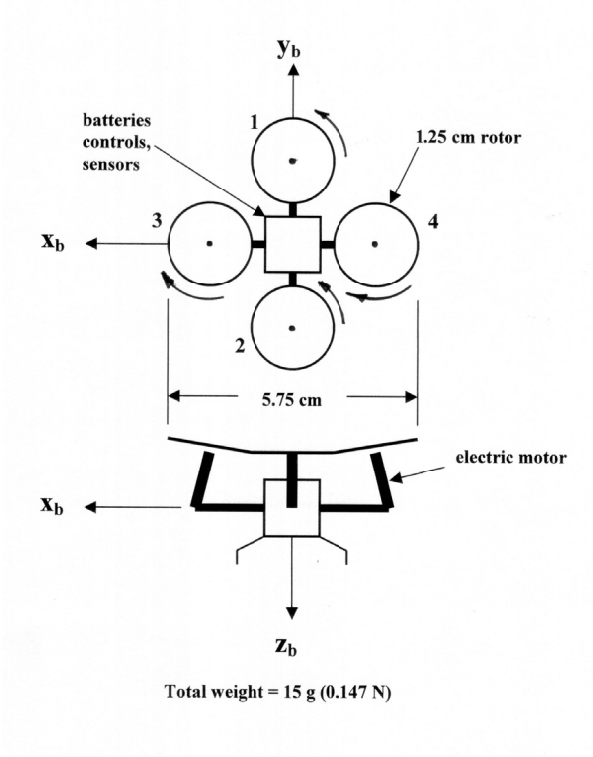

Figure 46 A notional model of a mesicotper

[1] SI units have been used in the description of the mesicopter model to conform to the original vehicle descriptions in [35].

The SMC design steps in Section 3 were followed as described below.

(1) The vehicle and motor dynamics have been obtained as described above. The electric motors were modelled as second-order "actuators" with both amplitude and rate limiting in terms of angular velocities and accelerations.

(2) A MIMO control system is to be designed. Here, pitch-rate and z-body axis velocity were the output variables of interest.

(3) Sliding manifolds were created for each of the control axes. The resulting controllers for each loop are identical and given by:

$$u(s) = \rho\left[1 + \frac{2}{s}\right]e(s) \tag{34}$$

where for the pitch-rate loop,

$$\rho = 632 \tag{35}$$

and for the z-body-axis velocity loop,

$$\rho = -3.724 \cdot 10^4 \tag{36}$$

(4) Sliding behaviour was validated in a computer simulation. The controllers exhibited crossover frequencies of 200 rad/sec.

(5) Boundary layers of unity thickness were implemented, eliminating the infinite-frequency switching.

(6) The system was unstable when the motor dynamics (actuators) were included.

(7) A single asymptotic observer was created to service both of the control loops. In designing the observer, it was assumed that the following measured variables were available, pitch-rate, x-body fixed axis velocity, z-body fixed-axis velocity. The state-space model used to obtain the observer was a minimum realization of the original seven-state vehicle model. The minimum realization resulted in a four-state model. The observer eigenvalues (four) were selected as λ = -20, -20.1, -20.2, -20.3. Figure 47 shows the equivalent, unity feedback loop transmission for the z-body axis velocity loop. Note that the crossover frequency has been considerably reduced from 200 rad/sec to 42.9 rad/sec through the action of the observer. The equivalent unity feedback loop transmission for the pitch-rate loop exhibited an identical crossover frequency with similar stability margins.

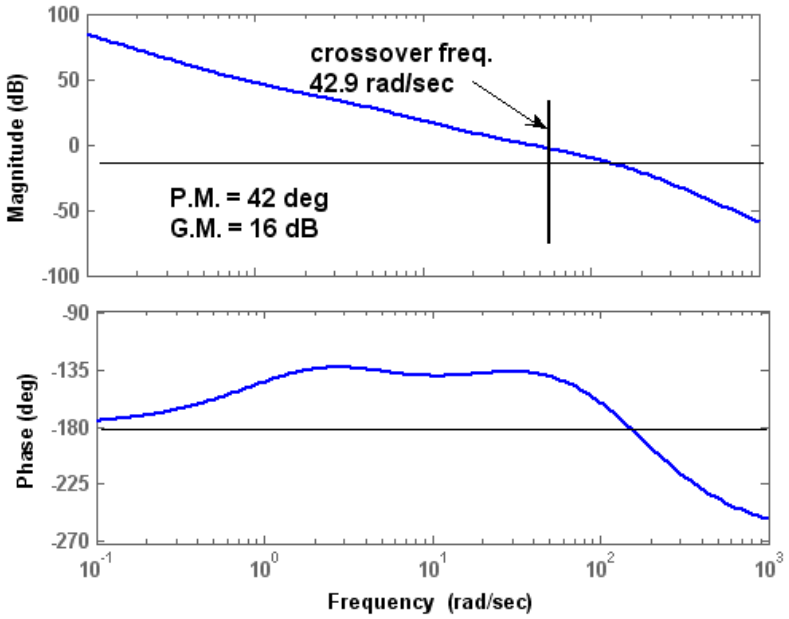

Figure 47 The equivalent, unity feedback loop transmission for the mesicopter z-body axis rate loop

(8) For simplicity, no reference model hedging was employed in the design.

(9) Since only flight about hover was considered, no scheduling of the observer was undertaken.

5.5.2 Computer Simulation

A simulation of the control design was undertaken. No additional outer-loop closures were considered. The test inputs were filtered doublets in pitch-rate command and z-body fixed axis velocity command. The magnitude of the doublets was 0.1 rad/sec for pitch-rate, and 0.1 m/sec z-body fixed axis velocity. Each pulse of the doublet lasted 5 sec. Sensor noise was included on each of the measure variables. The RMS noise levels were 0.1 deg/sec for pitch-rate, and $1 \cdot 10^{-3}$ m/sec for x and z-body axis velocities. Finally, horizontal turbulence was included with an RMS value of 0.5 m/sec. The turbulence inputs were included as variations in tip-speed ratio [36] of the rotors in the original, nonlinear model. Figures 48 and 49 show the commands and vehicle responses. Figure 50 shows the change in the RPM for rotor 1 from the trim value of 3,689 RPM.

Finally, mesicopter "damage" was modelled by a 25% reduction in the magnitude of the RPM commands to all the motors and inclusion of a 0.015 sec time delay before each motor input. Figures 51 – 53 show the system performance. With the exception of minor differences between the responses of Figs. 48 and 51, little in the way of performance degradation is noted.

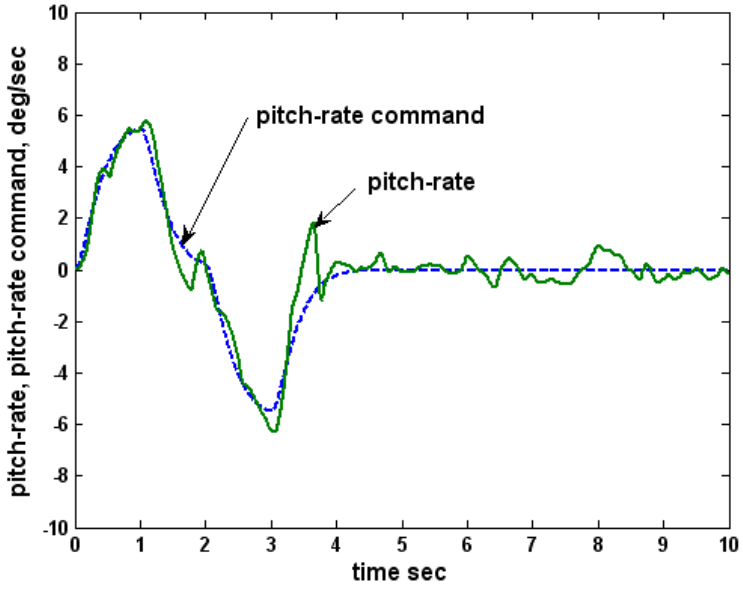

Figure 48 Mesicopter pitch-rate performance

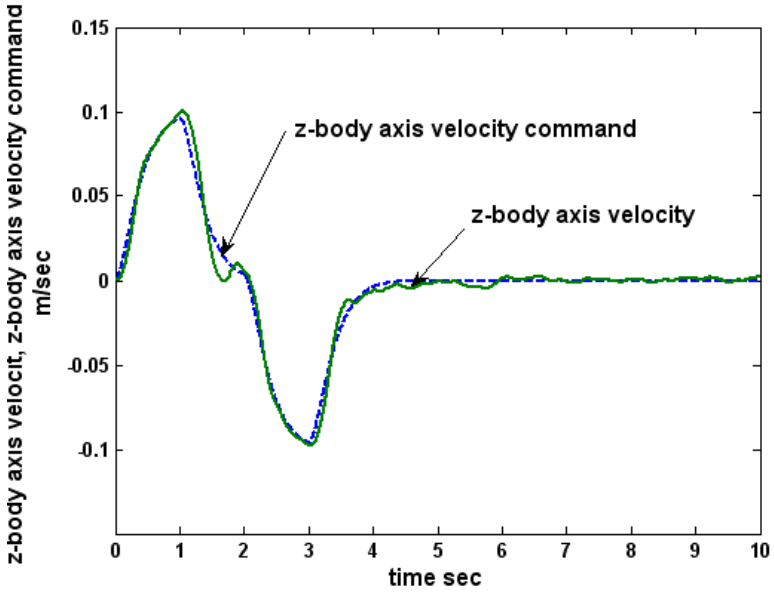

Figure 49 Mesicopter z-body axis velocity performance

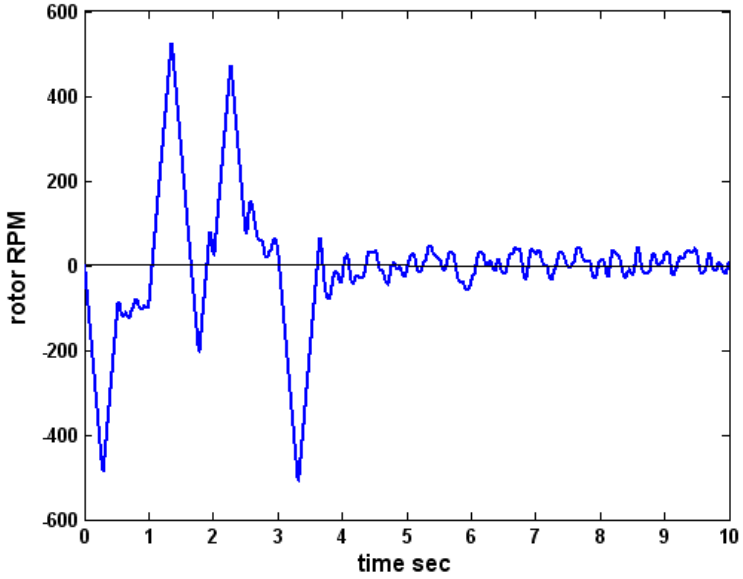

Figure 50 Change in rotor 1 RPM from trim

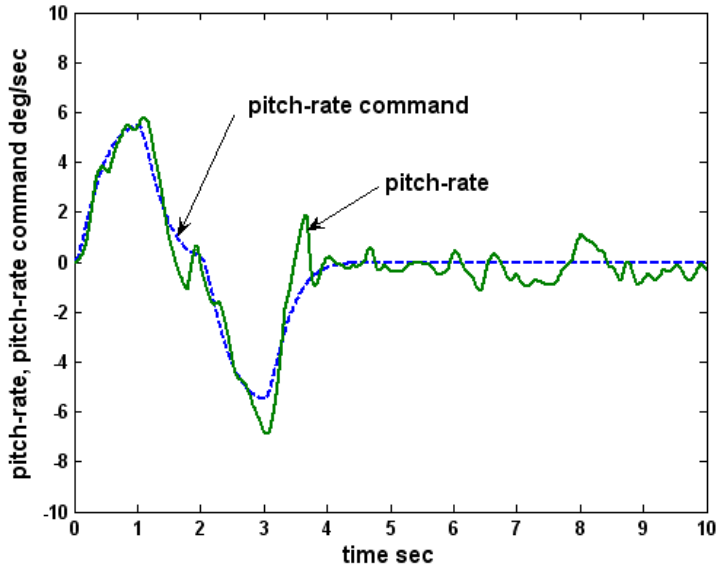

Figure 51 Mesicopter pitch-rate performance with modelled damage

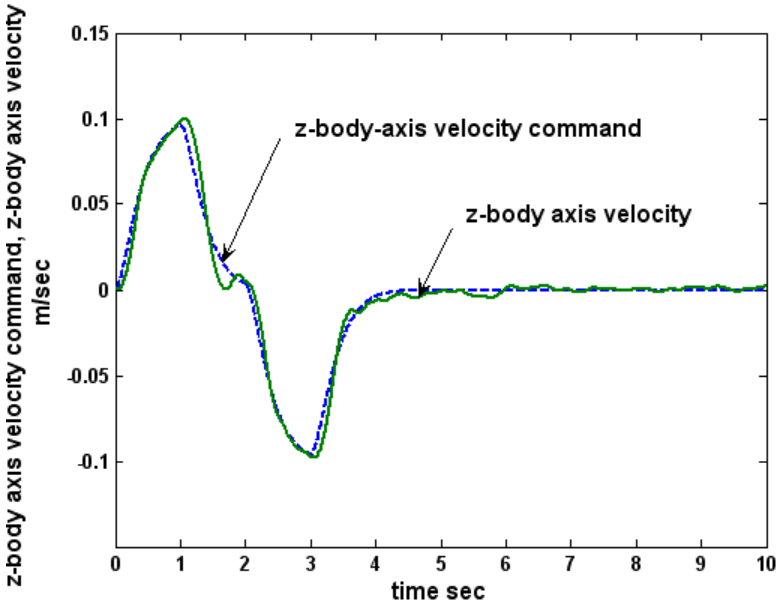

Figure 52 Mesicopter z-body axis velocity performance with modelled damage

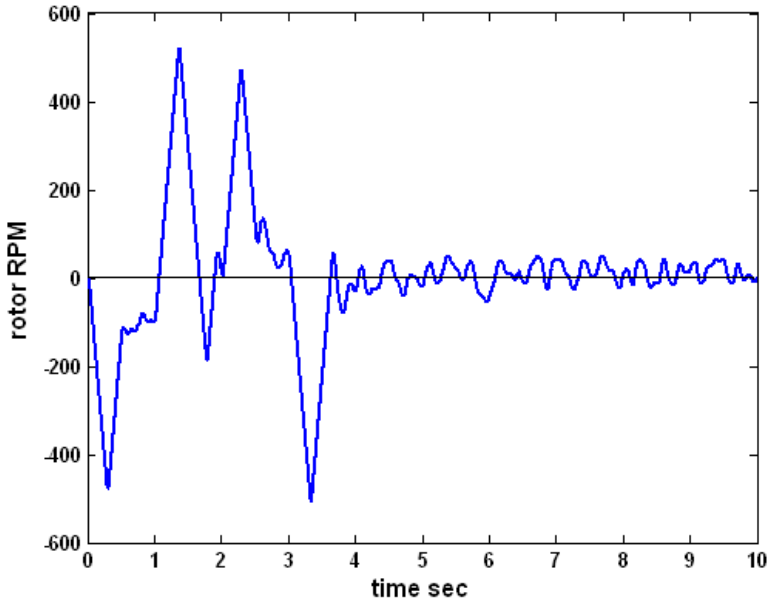

Figure 53 Change in rotor 1 RPM from trim with modelled damage

Some insight into the characteristics of the SMC design can be obtained by considering the equivalent, unity-feedback loop transmission for the z-body axis velocity loop. Here the Bode diagrams for three equivalent loop transmissions will be compared. The first, denoted L_{eq} nominal, is identical to the loop transmission of Fig. 47. The second, denoted L_{eq} damaged, is the equivalent loop transmission with the 25% reduction in gain and time delay introduction. The third, denoted L_{eq} static, is obtained as

$$L_{eq}\,\text{static} = (L_{eq}\,\text{nominal})(0.75)e^{-0.015s} \tag{37}$$

Figure 54 results. Note that, for clarity, the frequency range has been reduced from that of Fig. 46. What is apparent form Fig. 54 is that the SMC design results in an equivalent, unity-feedback loop transmission that is significantly different than that obtained by introducing the gain and time delay variations on the loop transmission in which there was no "damage". Note that, although the L_{eq} damaged displays a crossover frequency reduction of approximately 0.5, the phase lags have been considerably reduced over that for L_{eq} static. This results in a significant increase in stability margins. This property can be likened to effective instantaneous "reconfiguration". That is, if one were to design a controller in which compensation was limited to the forward loop, an instantaneous change in this compensation would be required to replicate the performance exhibited by the SMC design. Similar results were demonstrated in [32].

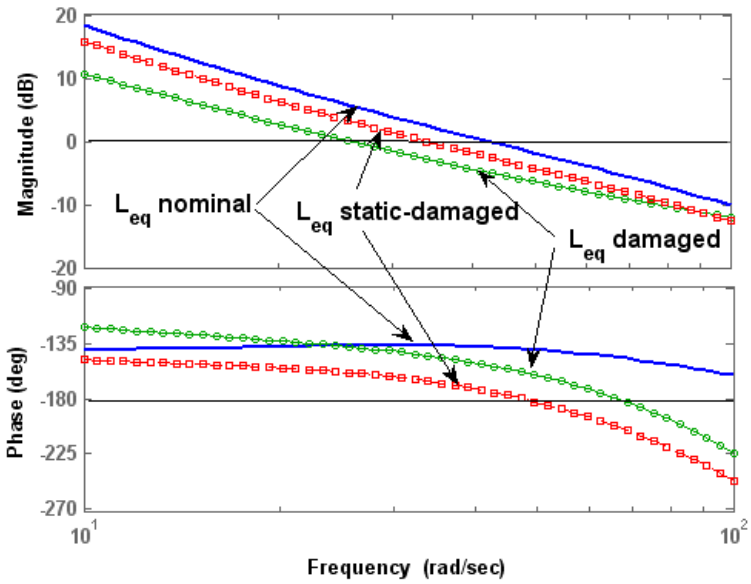

Figure 54 Comparison of equivalent, unity-feedbak loop transmissions for mesicopter z-body axis velocity loop

6.0 DISCUSSION

The material presented in the preceding five sections has been an attempt at demonstrating the applicability of

a frequency-domain based, pseudo-sliding mode control synthesis technique for robust flight control system design. The examples have ranged from designs for a large, flexible bomber weighing some 288,000 pounds to a near "nano-scale" vehicle weighing 0.53 oz. The functions required of a successful flight control system design that were outlined in Section 1 have been met, to some extent, in each of the examples considered. There are a number of critiques of the design procedure that should be discussed, if only briefly.

6.1 Stability Proofs

Noticeably absent from the proposed design technique are proofs of stability. In SMC designs, this question is typically addressed through Lyapunov stability criteria with the goal of guaranteeing global attractiveness of the sliding manifold, i.e. the reaching condition, e.g., [37]. The interpretation of pseudo-sliding mode in the frequency-domain, as done here, merely means that *linear* stability can be ascertained through application of linear techniques such as the Nyquist criterion. Guaranteeing stability when the vehicle undergoes significant changes in dynamic characteristics, as was the case, for example, in the examples of Section 5.2 and 5.3, is quite difficult. This is attributable to the fact that the high-bandwidth nature of the SMC approach often results in rate saturation of the actuators, thus eliminating linear stability analyses. For example, Fig. 55 from [27] shows the actuator output rate for one of the ICE vehicle control effectors after the cumulative damage described in Table 3 of Section 5.2.3. Performance was excellent with this failure, however a proof of stability under this condition would be extremely difficult. The author has simply opted for computer simulation to demonstrate stability in these cases.

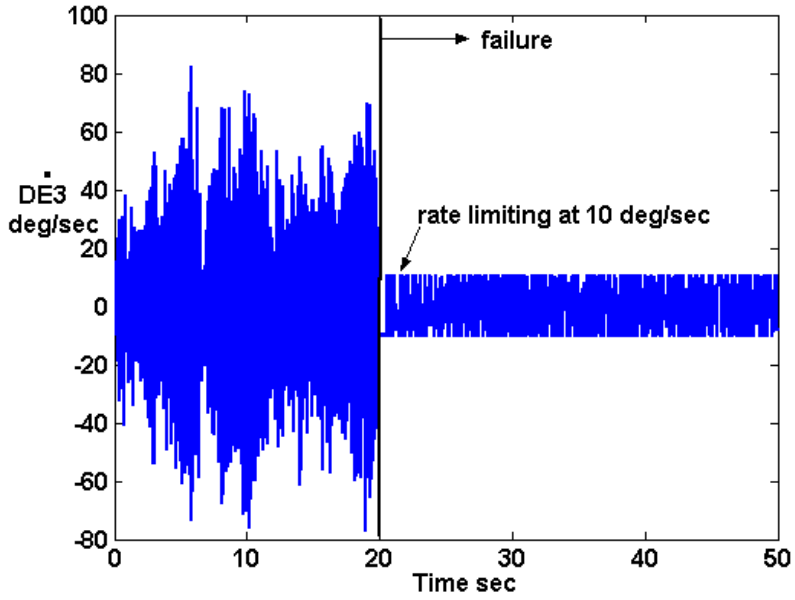

Figure 55 Actuator rate limiting after modelled failure, Mach No. = 0.9, Alt. = 35,000 ft, from [25]

6.2 Quantitative Design

Also absent from the design procedure is a *quantitative* approach to the design, driven by specific

performance requirements and model uncertainty, such as that found in Quantitative Feedback Theory (QFT) [3]. This shortcoming can again be traced to the nonlinear nature of the control activity that often results when the technique is applied to vehicles undergoing significant variations in dynamics due to modelled failures. This obviously remains an area of research. The primary design tradeoff that is involved is in the selection of observer eigenvalues and hedge systems. Large eigenvalues brings the design closer to a true SMC system with added robustness to variations in system dynamics. Large eigenvalues also increase the design's sensitivity to the parasitic dynamics of the actuators. Conversely, small observer eigenvalues "hide" the parasitic dynamics of the actuators, but at the cost of some robustness to variations in system dynamics.

6.3 Square Control System Architectures and Non-minimum Phase Transmission Zeros

The proposed design technique assumes square control system architectures where the number of controlled response variables equals the number of control (or pseudo-control) inputs. This, in itself, presents no significant difficulties, as multiple control effectors can be accommodated through control distribution matrices. Determining the form of the control distribution matrix is not always a trivial undertaking. Approaches can vary from the formal pseudo-inverse technique of [27] to an ad hoc approach in which effectors are assigned to specific response variables with relative gains selected in proportion to the amplitude or rate limits of the actuator driving the effector, e.g., [38]. One approach to the input/output pairing problem for square control system architectures is provided in [39].

The existence of low-frequency, non-minimum phase transmission zeros pose a significant problem for the design approach, as the relatively high-gain nature of the SMC design will create input/output zeros very near the transmission zeros [39], and indeed drive closed-loop poles into the right-half plane. The existence of these unstable modes may be difficult to establish in computer simulation due to the small residues that result. The use of "regulated variables" to eliminate the non-minimum phase transmission zeros provides one solution to this problem [38]. The examples herein that involved pure time delays in failed or "damaged" modes owed their stability to the existence of the observer(s) and to the fact that the zeros were far into the right half plane.

6.3 Measurement Noise

The high-bandwidth nature of the SMC design approach makes it sensitive to the effects of sensor or measurement noise. This was evident in all the examples. The resulting control activity is simply the price that must be paid for the robustness that the design approach offers. The first example involving the flexible aircraft, was deliberately included to demonstrate that the increased control activity does not necessarily prevent application to vehicles with aeroelastic modes.

7.0 SUMMARY AND ACKOWLEDGMENTS

A frequency-domain based approach to the design of sliding-mode flight control systems has been discussed and a number of applications considered. In the context of this discussion, the sliding-mode technique served essentially as a means to an end, that being the synthesis of flight control systems that exhibited stability and performance robustness in the presence of significant variations in the vehicle dynamics. Since a majority of potential applications of this technique may be to piloted vehicles, some attention has been paid to the description of a control-theoretic model of the human pilot that can be used in compute simulation of the complete piot/vehicle system. The caveats outlined in Section 6 should be borne in mind in any application of the proposed technique. The proposed design approach may be particularly advantageous when applied to

"nano-scale" UAVs, where on-board computational power may be limited, and where even minor vehicle damage may be enough to cause instability.

A number of the examples reported herein were the results of research performed by graduate students in the Dept. of Mechanical and Aeronautical Engineering, at the University of California, Davis, under the supervision of the author. The students involved were Lt. Col. Scott Wells (Ph.D. 2002), Mr. Travis Vetter (MS 2002), Mr. Troy Ussery (MS 2003), Ms. Christina Spaulding (MS 2005), and Ms. Maryam Bakjtiari-Nejad (MS 2006). The research summarized herein would not have been possible without the contributions of these students.

REFERENCES

[1] McRuer, D., Ashkenas, I, and Graham, D., *Aircraft Dynamics and Automatic Control,* Princeton University Press, Princeton, NJ, 1973.

[2] Houpis, C. H., "Horowitz: bridging the gap," *International Journal of Robust and Nonlinear Control,* Vol. 12, No. 4, pp. 295-302, 2002.

[3] Horowitz, I., *Quantitative Feedback Theory, Vol. 1*, QFT Publications, Boulder, 1993.

[4] Steinberg, M., "Historical Overview of Research in Reconfigurable Flight Control," *Journal of Aerospace Engineering,* Vol. 219, No. G4, 2005, pp 263-276.

[5] Wells, S. R., "Application of Sliding Mode Methods to the Design of Reconfigurable Flight Control Systems, Ph.D. Dissertation, Dept. of Mechanical and Aeronautical Engineering, University of California, Davis, CA., 2002.

[6] Young, K. D., Utkin, V. I., and Özguner, U, "A Control Engineer's Guide to Sliding Mode Control," *IEEE Transactions on Control Systems Technology,* Vol. 7, No. 3, 1999, pp. 328-342.

[7] McRuer, D. Graham, D, Krendel, E., and Reisener, W. Jr., "Human Pilot Dynamics in Compensatory Systems, Theory, Models and Experiments with Controlled Element and Forcing Function Variations," Air Force Flight Dynamics Laboratory, AFFDL-TR-65-15, 1965.

[8] Maciejowski, J. M., *Multivariable Feedback Design,* Addison-Wesley, Wokingham, England, 1989, Chap. 1.

[9] Itkis, U., *Control Systems of Variable Structure,* Wiley, New York, 1976.

[10] Utkin, V. I., Variable structure systems with sliding mode, *IEEE Transactions on Automatic Control,* Vol. AC-22, 1977, pp. 212-222.

[11] Edwards, C. and Spurgeon, S. K., *Sliding Mode Control*, Taylor & Francis, London, 1998.

[12] Slotine, J. J. E and Li, W., *Applied Nonlinear Control,* Prentice Hall, Englewood Cliffs, New Jersey, 1991.

[13] Wells, S. R. and Hess, R. A., MIMO Sliding mode control for a tailless fighter, *Journal of Guidance,*

Control, and Dynamics, Vol. 26, No. 3, 2003, pp. 463-473.

[14] Saberi, A., Chen, B. M. and Sannuti, P., *Loop Transfer Recovery: Analysis and Design (Communication and Controls Engineering),* Springer, New York, 1993.

[15] Vetter, T. K., Wells, S. R., and Hess, R. A. "Designing for Damage – Robust Flight Control Design Using Sliding Mode Techniques," *Journal of Aerospace Engineering,* Vol. 217, No. G5, 2003, pp. 245-262.

[16] Hoh, R. H., and Mitchell, D. G., "Handling-Qualities Specification – A Functional Requirement for the Flight Control System," in *Advances in Aircraft Flight Control,* Ed: M. B. Tischler, Taylor and Francis, London, 1996, Chap. 1.

[17] Hess, R. A., "Unified Theory for Aircraft Handling Qualities and Adverse Aircraft-Pilot Coupling," *Journal of Guidance, Control, and Dynamics,* Vol. 20, No. 6, 1997, pp. 1141-1148.

[18] Hess, R. A., "A Model of the Human's Use of Motion Cues in Vehicular Control," *Journal of Guidance, Control, and Dynamics,* Vol. 13, No. 3, 1990, pp. 476-482.

[19] McRuer, D. T., and Magdaleno, R. E., "Experimental Validation and Analytical Elaboration for Models of the Pilot's Neuromuscular Subsystem in Tracking," NASA CR-1757, 1971.

[20] van Paasen, M. M., van der Vaart, J. C., and Mulder, J. A., "Model of the Neuromuscular Dynamics of the Human Pilot's Arm," *Journal of Aircraft,* Vol., 41, No. 6, 2004, pp. 1482-1490.

[21] Hess, R. A., Zeyada, Y., and Heffley, R. K., "Modeling and Simulation for Helicopter Task Analysis," *Journal of the American Helicopter Society,* Vol. 47, No. 4, 2002, pp. 243-242.

[22] Hess, R. A., "Simplified Technique for Modeling Piloted Rotorcraft Operations Near Ships," *Journal of Guidance, Control, and Dynamics,* Vol. 29, No. 6, 2006, pp. 1339-1349.

[23] Waszak, M. and Schmidt, D. K., "Flight Dynamics of Aeroelastic Vehicles," *Journal of Aircraft,* Vol. 15, No. 6, 1988, pp. 563-571.

[24] Waszak, M. R. Davidson, J. B., and Schmidt, D. K., "A Simulation Study of the Flight Dynamics of Elastic Aircraft," NASA CR 4102, Vols. One and Two, Dec. 1987.

[25] Hess, R. A., "Identification of Pilot-Vehicle Dynamics From Simulation and Flight Test," *Control and Dynamic Systems, Vol. 33, Advances in Aerospace Systems Dynamics and Control Systems*, Edited by C. T. Leondes, Academic Press, London, 1990, pp. 151-175.

[26] Mitchell, D.G. Aponso, B. L, and Klyde, D. H., "Effects of Cockpit Lateral Stick Characteristics on Handling Qualities and Pilot Dynamics," NASA CR 4443, June 1992.

[27] Hess, R. A., Vetter, T. K., and Wells, S. R., "Design and Evaluation of a Damage-Tolerant Flight Control System," *Journal of Aerospace Engineering,* Vol. 219, No. G4, 2005, pp. 341-360.

[28] Pate, A. B., and Steinberg, M. L., "A Closed-Loop Comparison of Control Allocation Methods, AIAA Paper No. 2000-4538, AIAA Guidance, Navigation, and Control Conference, August, 2000. Denver, CO.

[29] Mitchell, D. G., Hoh, R., Aponso, B. L., and Klyde, D. H., "Proposed Incorporation of Mission-Oriented Flying Qualities into MIL-STD-1797A," Wright Aeronautical Laboratory, WL-TR-94-3162, 1994.

[30] Hess, R. A. and Bakhtiari-Nejad, M., "Sliding Mode Control of a Nonlinear Ducted-Fan UAV Model," AIAA Paper No. 2006-6088, AIAA Guidance, Navigation, and Control Conferencd and Exhibit, August, 2006, Keystone, CO.

[31] Spaulding, C. M., Mansur, M. J., Tischler, M. B., Hess, R. A., and Franklin, J. A., "Nonlinear Inversion Control for a Ducted Fan UAV," AIAA Paper No. 2005-6231, AIAA Atmospheric Flight Mechanics Conference, August, 2005, San Francisco, CA.

[32] Hess, R. A., and Ussery, T. M., "Frequency-Domain Sliding Mode Design Technique Applied to the Control of a Ducted Fan Micro-Air Vehicle," *Journal of the American Helicopter Society,* Vol. 49, No. 1, 2004, pp. 457-467.

[33] Colbourne, J. D., Frost, C. R., Tischler, Cheung, K. K., Hiranaka, D. K., and Biezad, D.J., "Control Law Design and Optimization for Rotorcraft Handling Qualities Using CONDUIT," American Helicopter Society 55th Annual Forum, August, 1999, Quebec, Canada.

[34] Kroo, I., and Kunz, P., "Meso-scale Flight and Miniature Rotorcraft Development," in *Fixed and Flapping Wing Aerodynamics for Micro Air Vehicle Applications,* Editor: T. Mueller, AIAA Progress in Astronautics and Aeronautics Series, V-195, 2001, Chap. 23.

[35] Kroo, I., Shantz, M., Kunz, P., Fay, G., Cheng, S., Fabian, T., Partridge, D., "The Mesicopter: A Miniature Rotorcraft Concept, Phase II Interim Report," http://www-rpl.stanford.edu/files/report/Interim_Report_Phase2.pdf, July 2000.

[36] Prouty, R. W., *Helicpopter Performance, Stability and Control,* PWS Engineering, Boston, 1986.

[37] DeCarlo, R., A., Zak, S. H., and Drakunov, S. V., "Section 57.5: Variable Structure, Sliding Mode Design," *The Control Handbook,* Ed: W. S. Levine, CRC Press, Inc., Boca Raton, 1996, pp. 941-951.

[38] Snell, A., "Decoupling Control Design with Applications to Flight," *Journal of Guidance, Control, and Dynamics,* Vol. 21, No. 4, 1998, pp. 647-655.

[39] Hess, R. A., "Coupling Numerators and Input-Output Pairing in Square Control Systems," *Journal of Guidance, Control, and Dynamics,* Vol. 26, No. 2, 2003, pp. 367-369.